

Holographic Anisotropic Model for Heavy Quarks in Anisotropic Hot Dense QGP with External Magnetic Field

Irina Ya. Aref'eva^a, Kristina Rannu^a and Pavel Slepov^a

^a*Steklov Mathematical Institute, Russian Academy of Sciences,
Gubkina str. 8, 119991, Moscow, Russia*

E-mail: arefeva@mi-ras.ru, rannu-ka@rudn.ru, slepov@mi-ras.ru

ABSTRACT: We present a five-dimensional fully anisotropic holographic model for heavy quarks supported by Einstein-dilaton-three-Maxwell action; one of the Maxwell fields is related to an external magnetic field. Influence of the external magnetic field on the 5-dim black hole solution and the confinement/deconfinement phase diagram is considered. The effect of the inverse magnetic catalyses is revealed and positions of critical end points are found.

KEYWORDS: AdS/QCD, holography, phase transition, Wilson loops, heavy quarks, magnetic field

Contents

1	Introduction	2
2	Model	4
2.1	Metric and EOM	4
2.2	Solution for heavy quarks model	6
3	Thermodynamics	12
3.1	Temperature and entropy	12
3.2	Free energy and background phase transition	15
3.3	Temporal Wilson loops	17
4	Conclusions	24
5	Acknowledgments	26
A	EOM	27
B	Tables	29
B.1		30
B.2		31

1 Introduction

Isotropic holographic QCD (HQCD) models, see for review [1–3], were considered in numerous papers [4]–[52]. These models have been considered to study the confinement/deconfinement phase transition [4–6, 9, 11, 14–19, 21, 29, 30, 33, 36, 46, 50–52], as well as the chiral phase transition [13, 20, 22, 31, 32, 38, 39, 41, 45, 46, 48] and also to search for quarkyonic phase transition [35]. One of the popular methods for constructing an HQCD is a potential reconstruction method for models with Einstein-dilaton-Maxwell action. It consists in starting with a given form of metric, which is a deformed form AdS_5 [3, 19], and then finding the dilaton potential that supports the given form of the metric. Metric deformation is realized by the warp factor, which in turn determines the blackening function and, consequently, the thermodynamics of the model. Choice of the warp factor in the metrics strongly influences the phase transition structure of HQCD. As a guiding principle in the choice of the warp factor one usually uses the agreement with the main features of lattice results. Unfortunately lattice cannot provide us a full picture of the QCD phase diagram and shows only its individual parts. The absence of general scheme of study different regimes in QCD is the origin to develop holographic approach to QCD. It occurred that the phase diagram describing heavy quarks can be obtained via deformation of AdS_5 by warp factor that is the exponential of a polynomial on holographic coordinate. For the simplest quadratic polynomial [4, 19] the model reproduces some features of phase diagram describing heavy quarks, meanwhile to reproduce phase diagram of light quarks one has to use rational functions [9, 26].

It was recognized that [12] it is important to add anisotropy in the holographic theory as QGP is an anisotropic media just after the HIC, and an estimation for isotropisation time is about $1\text{--}5\text{ fm}/c \sim 10^{-24}\text{ s}$ [68]. To deal with anisotropic HQCD one considers Einstein-dilaton-two Maxwell model with additional Maxwell field to support the anisotropy in metrics. Such anisotropic model was considered in [28] for heavy quarks and in [44] for light quarks. In these models anisotropy is defined by a parameter ν , and its value of about $\nu = 4.5$ gives the dependence of the produced entropy on energy in accordance with the experimental data for the energy dependence of the total multiplicity of particles created in heavy ion collisions [69]. Isotropic holographic models had not been able to reproduce the experimental multiplicity dependence on energy ([70] and refs therein). As shown in [30], the model [28] describes smeared confinement/deconfinement phase transitions. This happens since the location on phase diagram of confinement/deconfinement transition line depends on orientation of quark pair in respect to the collision line. That model also indicates the relations of the fluctuations of the multiplicity, i.e. the entanglement entropy, with the background phase transitions [71]. More precisely, the fluctuations of entropy are directly related to the background phase transition, and points to the

locations of chiral symmetry breaking. Only in particular cases, when the decay of small black holes to large ones throws out the stable phase to the zone with no dynamical wall, the background phase transition is also the confinement/deconfinement transition. In more general cases, as it has stressed in [49], entanglement entropy is sensitive to mass gap, i.e. the correlation length. Note that anisotropy of the background metric also influences on corresponding jet quenching [12, 72, 73].

There also is another source of anisotropy – an external magnetic field. Strong magnetic field in the physical 4-dimensional space-time appears in non-central HIC [56–60]. This external magnetic field presents another type of anisotropy and the phenomenon of magnetic catalysis (MC)/inverse magnetic catalysis (IMC) is associated with it. Strong magnetic fields are present in neutron stars and magnetars [63, 64], as well as in the early cosmology [61, 62]. So it is important to take into account this anisotropy in the holographic approach. This anisotropy for improved holographic QCD with Maxwell action has been considered in [18, 23, 34, 40] and for the model with a stack of branes in the Veneziano limit in [74–76].

In this paper we present a fully anisotropic holographic model for heavy quarks. It is set up by Einstein-dilaton-three-Maxwell action. This model describes two different types of anisotropy: anisotropy for producing the multiplicity dependence on energy (this type of anisotropy is supported by the 2nd Maxwell field in action) and anisotropy connected with the magnetic field (this type is supported by 3rd Maxwell field). The 1st Maxwell field is introduced to describe chemical potential. We start from a deformed anisotropic metric and recover the dilaton potential and some of kinetic gauge functions from the Einstein-dilaton Maxwell equations. The form of deformation is chosen to reproduce a typical for heavy quarks phase structure, supported by lattice calculations. Deformation of the metric for light quarks is different [14, 26, 44], and this agrees with so-called Columbia plot [53–55].

This paper is organised as follows. In Sect.2 the 5-dim holographic model of hot dense anisotropic QCD in magnetic field is presented. In Sect.2.1 action and metric to set up the model are introduced and in Sect.2.2 the corresponding 5-dim BH solution reconstructing heavy quarks model is discussed. Sect.3 contains thermodynamic properties of the model in external magnetic field: temperature and entropy behavior (Sect.3.1), magnetic field influence on the solution properties following from the free energy – the lifetime of the unstable state and BH-BH phase transition picture (BH-BH phase transition curve and critical end points positions) (Sect.3.2), temporal Wilson loops and crossover regions on the phase diagram with magnetic field (Sect.3.3). The main conclusions of this investigation and subjects for further research are given in Sect.4. Details on magnetic field setting and following EOM handling are given in Appendix A. A review of holographic heavy quarks

models with different polynomial warp-factors for zero and non zero magnetic field are presented in appendices B.1 and B.2 respectively.

2 Model

2.1 Metric and EOM

We take the action in Einstein frame

$$S = \frac{1}{16\pi G_5} \int d^5x \sqrt{-g} \times \left[R - \frac{f_1(\phi)}{4} F^{(1)2} - \frac{f_2(\phi)}{4} F^{(2)2} - \frac{f_B(\phi)}{4} F^{(B)2} - \frac{1}{2} \partial_\mu \phi \partial^\mu \phi - V(\phi) \right], \quad (2.1)$$

$$\begin{aligned} F_{\mu\nu}^{(1)} &= \partial_\mu A_\nu - \partial_\nu A_\mu, \text{ i.e. } A_\mu^{(1)} = A_t(z) \delta_\mu^0, \\ F_{\mu\nu}^{(2)} &= q \, dy^1 \wedge dy^2, \text{ i.e. } F_{y_1 y_2}^{(2)} = q, \\ F_{\mu\nu}^{(B)} &= q_B \, dx \wedge dy^1, \text{ i.e. } F_{xy_1}^{(B)} = q_B. \end{aligned} \quad (2.2)$$

where $\phi = \phi(z)$ is the scalar field, $f_1(\phi)$, $f_2(\phi)$ and $f_B(\phi)$ are the coupling functions associated with the Maxwell fields A_μ , $F_{\mu\nu}^{(2)}$ and $F_{\mu\nu}^{(B)}$ correspondingly, q and q_B are constants and $V(\phi)$ is the scalar field potential. Thus (2.1) is the extended version of the action used in [28, 44], where we add an external magnetic field $F_{\mu\nu}^{(B)}$ ¹.

To consider action (2.1) let us take the ansatz in the following view:

$$ds^2 = \frac{L^2}{z^2} \mathbf{b}(z) \left[-g(z) dt^2 + dx^2 + \left(\frac{z}{L} \right)^{2-\frac{2}{\nu}} dy_1^2 + e^{c_B z^2} \left(\frac{z}{L} \right)^{2-\frac{2}{\nu}} dy_2^2 + \frac{dz^2}{g(z)} \right], \quad (2.3)$$

$$\mathbf{b}(z) = e^{2\mathcal{A}(z)}, \quad (2.4)$$

where L is the AdS-radius, $\mathbf{b}(z)$ is the warp-factor, $\mathcal{A}(z)$ is related with $\mathbf{b}(z)$ according (2.4), $g(z)$ is the blackening function, ν is the parameter of primary anisotropy, caused by non-symmetry of heavy-ion collision (HIC), and c_B is the coefficient of secondary anisotropy related to the external magnetic field $F_{\mu\nu}^{(B)}$. Choice of $\mathcal{A}(z)$ determines the heavy/light quarks description of the model, so we follow previous works and consider $\mathcal{A}(z) = -cz^2/4$ for heavy quarks [28] and $\mathcal{A}(z) = -a \ln(bz^2 + 1)$ for light-quarks [44].

¹There also exists another choice of $F_{\mu\nu}^{(B)}$ -field different from $F_{\mu\nu}^{(2)}$. The corresponding EOM can be found in Appendix A.

The corresponding EOM have the form ²

$$\begin{aligned} \phi'' + \phi' \left(\frac{g'}{g} + \frac{3\mathfrak{b}'}{2\mathfrak{b}} - \frac{\nu+2}{\nu z} + c_B z \right) + \left(\frac{z}{L} \right)^2 \frac{\partial f_1}{\partial \phi} \frac{(A_t')^2}{2\mathfrak{b}g} - \left(\frac{L}{z} \right)^{2-\frac{4}{\nu}} \frac{\partial f_2}{\partial \phi} \frac{q^2 e^{-c_B z^2}}{2\mathfrak{b}g} - \\ - \left(\frac{z}{L} \right)^{\frac{2}{\nu}} \frac{\partial f_B}{\partial \phi} \frac{q_B^2}{2\mathfrak{b}g} - \left(\frac{L}{z} \right)^2 \frac{\mathfrak{b}}{g} \frac{\partial V}{\partial \phi} = 0, \end{aligned} \quad (2.5)$$

$$A_t'' + A_t' \left(\frac{\mathfrak{b}'}{2\mathfrak{b}} + \frac{f_1'}{f_1} + \frac{\nu-2}{\nu z} + c_B z \right) = 0, \quad (2.6)$$

$$g'' + g' \left(\frac{3\mathfrak{b}'}{2\mathfrak{b}} - \frac{\nu+2}{\nu z} - c_B z \right) - 2g \left(\frac{3\mathfrak{b}'}{2\mathfrak{b}} - \frac{2}{\nu z} - c_B z \right) c_B z - \left(\frac{z}{L} \right)^2 \frac{f_1 (A_t')^2}{\mathfrak{b}} = 0, \quad (2.7)$$

$$\mathfrak{b}'' - \frac{3(\mathfrak{b}')^2}{2\mathfrak{b}} + \frac{2\mathfrak{b}'}{z} - \frac{4\mathfrak{b}}{3\nu z^2} \left(1 - \frac{1}{\nu} + \left(1 - \frac{3\nu}{2} \right) c_B z^2 - \frac{\nu c_B^2 z^4}{2} \right) + \frac{\mathfrak{b} (\phi')^2}{3} = 0, \quad (2.8)$$

$$2g' \frac{\nu-1}{\nu} + 3g \frac{\nu-1}{\nu} \left(\frac{\mathfrak{b}'}{\mathfrak{b}} - \frac{4(\nu+1)}{3\nu z} + \frac{2c_B z}{3} \right) + \left(\frac{L}{z} \right)^{1-\frac{4}{\nu}} \frac{L q^2 e^{-c_B z^2} f_2}{\mathfrak{b}} = 0, \quad (2.9)$$

$$\begin{aligned} \frac{\mathfrak{b}''}{\mathfrak{b}} + \frac{(\mathfrak{b}')^2}{2\mathfrak{b}^2} + \frac{3\mathfrak{b}'}{\mathfrak{b}} \left(\frac{g'}{2g} - \frac{\nu+1}{\nu z} + \frac{2c_B z}{3} \right) - \frac{g'}{3zg} \left(5 + \frac{4}{\nu} - 3c_B z^2 \right) + \frac{8}{3z^2} \left(1 + \frac{3}{2\nu} + \frac{1}{2\nu^2} \right) - \\ - \frac{4c_B}{3} \left(1 + \frac{3}{2\nu} - \frac{c_B z^2}{2} \right) + \frac{g''}{3g} + \frac{2}{3} \left(\frac{L}{z} \right)^2 \frac{\mathfrak{b}V}{g} = 0, \end{aligned} \quad (2.10)$$

where $' = \partial/\partial z$ and

$$f_B = 2 \left(\frac{z}{L} \right)^{-\frac{2}{\nu}} \mathfrak{b}g \frac{c_B z}{q_B^2} \left(\frac{3\mathfrak{b}'}{2\mathfrak{b}} - \frac{2}{\nu z} + c_B z + \frac{g'}{g} \right). \quad (2.11)$$

We use the boundary conditions [44]:

$$A_t(0) = \mu, \quad A_t(z_h) = 0, \quad (2.12)$$

$$g(0) = 1, \quad g(z_h) = 0, \quad (2.13)$$

$$\phi(z_0) = 0. \quad (2.14)$$

where z_h is a size of horizon and z_0 is the integration boundary, $0 \leq z_0 \leq z_h$. Taking $z_0 = 0$ repeats consideration in [26] and $z_0 = z_h$ was used in [28]. The form of

²Note, that this is transformed EOM, for more details see Appendix A.

the integration boundary $z_0 = z_0(z_h)$ determines the string tension behavior in the model. This aspect was discussed in more details in [44, 51].

Excluding anisotropy and normalizing to the AdS-radius, i.e. putting $L = 1$, $\nu = 1$ and $f_2 = f_B = c_B = 0$ into (2.5)–(2.10), we get the expressions that fully coincide with the EOM (2.12)–(2.16) from [28].

2.2 Solution for heavy quarks model

To solve EOM (2.5–2.10) we first need to determine the form of the coupling function f_1 . To do this we base on our previous experience. In anisotropic heavy quarks [28] and light quarks models [44] we used the following expressions:

$$f_{1HQ} = z^{-2+\frac{2}{\nu}}, \quad f_{1LQ} = e^{-cz^2 - \mathcal{A}(z)} z^{-2+\frac{2}{\nu}}. \quad (2.15)$$

To describe heavy quarks' behavior holographically, let us take $\mathfrak{b} = e^{-\frac{cz^2}{2}}$ and $f_1 = z^{-2+\frac{2}{\nu}}$, therefore system (2.5–2.10) has the solution ³

$$A_t = \mu \frac{e^{\frac{1}{4}(c-2c_B)z^2} - e^{\frac{1}{4}(c-2c_B)z_h^2}}{1 - e^{\frac{1}{4}(c-2c_B)z_h^2}}, \quad (2.16)$$

$$g = e^{c_B z^2} \left\{ 1 - \frac{\Gamma\left(1 + \frac{1}{\nu}; 0\right) - \Gamma\left(1 + \frac{1}{\nu}; \frac{3}{4}(2c_B - c)z^2\right)}{\Gamma\left(1 + \frac{1}{\nu}; 0\right) - \Gamma\left(1 + \frac{1}{\nu}; \frac{3}{4}(2c_B - c)z_h^2\right)} - \frac{\mu^2 (2c_B - c)^{-\frac{1}{\nu}}}{4L^2 \left(1 - e^{(c-2c_B)\frac{z_h^2}{4}}\right)^2} \left(\Gamma\left(1 + \frac{1}{\nu}; 0\right) - \Gamma\left(1 + \frac{1}{\nu}; \frac{3}{4}(2c_B - c)z^2\right) \right) \times \right. \\ \left. \times \left[1 - \frac{\Gamma\left(1 + \frac{1}{\nu}; 0\right) - \Gamma\left(1 + \frac{1}{\nu}; \frac{3}{4}(2c_B - c)z^2\right)}{\Gamma\left(1 + \frac{1}{\nu}; 0\right) - \Gamma\left(1 + \frac{1}{\nu}; \frac{3}{4}(2c_B - c)z_h^2\right)} \frac{\Gamma\left(1 + \frac{1}{\nu}; 0\right) - \Gamma\left(1 + \frac{1}{\nu}; (2c_B - c)z_h^2\right)}{\Gamma\left(1 + \frac{1}{\nu}; 0\right) - \Gamma\left(1 + \frac{1}{\nu}; (2c_B - c)z^2\right)} \right] \right\}, \quad (2.17)$$

$$f_B = -2 \left(\frac{z}{L}\right)^{-\frac{2}{\nu}} e^{-\frac{1}{2}cz^2} \frac{c_B z}{q_B^2} g \left(\frac{3cz}{2} + \frac{2}{\nu z} - c_B z - \frac{g'}{g} \right), \quad (2.18)$$

$$f_2 = 4 \left(\frac{z}{L}\right)^{2-\frac{4}{\nu}} e^{-\frac{1}{2}(c-2c_B)z^2} \frac{\nu - 1}{q^2 \nu z} g \left(\frac{\nu + 1}{\nu z} + \frac{3c - 2c_B}{4} z - \frac{g'}{2g} \right), \quad (2.19)$$

$$\phi = \int_{z_0}^z \frac{1}{\nu \xi} \sqrt{4\nu - 4 + (4\nu c_B + 3(3c - 2c_B)\nu^2) \xi^2 + \left(\frac{3}{2}\nu^2 c^2 - 2c_B^2\right) \xi^4} d\xi, \quad (2.20)$$

³More general forms of $P(z)$ do not admit explicit express for A_t and g , and will be considered separately.

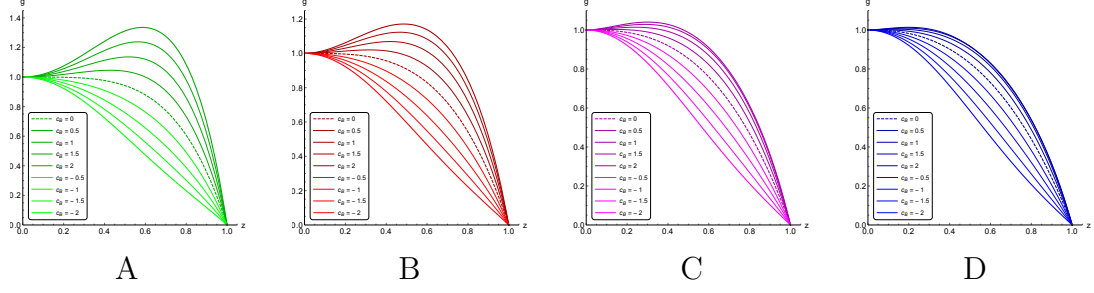


Figure 1. Blackening function $g(z)$ for different c_B for $\nu = 1$ (A), $\nu = 1.5$ (B), $\nu = 3$ (C), $\nu = 4.5$ (D); $c = 0.227$, $z_h = 1$, $\mu = 0$.

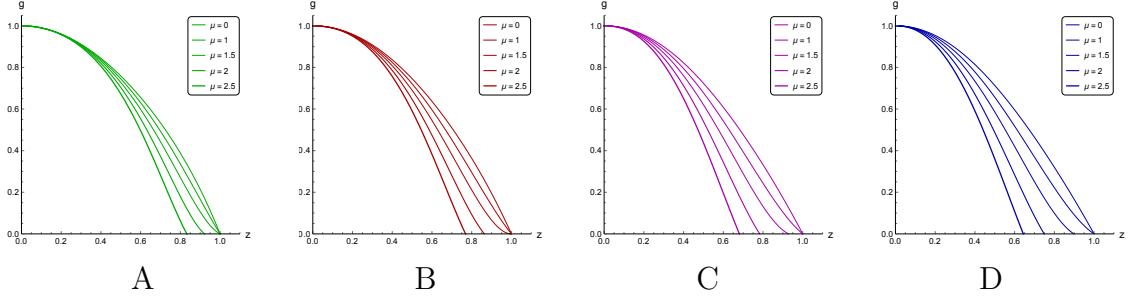


Figure 2. Blackening function $g(z)$ for different μ for $\nu = 1$ (A), $\nu = 1.5$ (B), $\nu = 3$ (C), $\nu = 4.5$ (D); $c = 0.227$, $z_h = 1$, $c_B = -1$.

$$\begin{aligned}
 V = -\frac{e^{\frac{1}{2}cz^2}}{4L^2\nu^2} \left\{ [8(1+2\nu)(1+\nu) + 2(3+2\nu)(3c-2c_B)\nu z^2 + (3c-2c_B)^2\nu^2 z^4]g - \right. \\
 \left. - [2(4+5\nu) + 3(3c-2c_B)\nu z^2]g' + 2g''\nu^2 z^2 \right\}.
 \end{aligned}
 \tag{2.21}$$

Note that the solution (2.16–2.21) was obtained for the external magnetic field set as $F_{xy_1}^{(B)} = q_B$.

To keep in touch not only with our previous model for heavy quarks [28], but also with our holographic description for light quarks [44] we assume $c = 0.227$.

As we can see from (2.17), blackening function doesn't actually depend on magnetic “charge” q_B , but it depends on coupling coefficient c_B , that characterises influence of the external magnetic field on metric along the y_2 -direction (Fig.1). Positive c_B causes the appearance of local maximum of the blackening function under the horizon. This maximum is expressed the brighter the higher the c_B value is. Negative c_B decreases the blackening function values till the horizon. Putting $c_B = 0$ brings us back to the previous model without the external magnetic field [28]. The only restriction on parameters' values that we obtain here is $c \neq 2c_B$, since for $c = 2c_B$ leads to singular behavior of curvature invariants.

We set $q_b = 1$ in most of the following calculations.

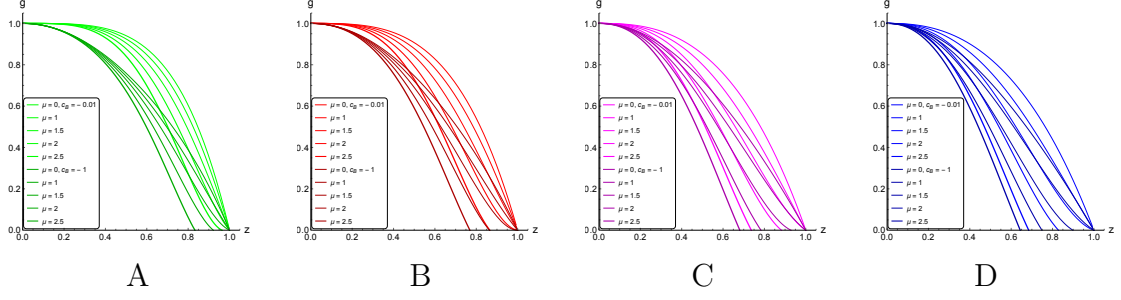


Figure 3. Blackening function $g(z)$ for different μ for $\nu = 1$ (A), $\nu = 1.5$ (B), $\nu = 3$ (C), $\nu = 4.5$ (D); $c = 0.227$, $z_h = 1$, $c_B = -0.01$ (light curves) and $c_B = -1$ (dark curves).

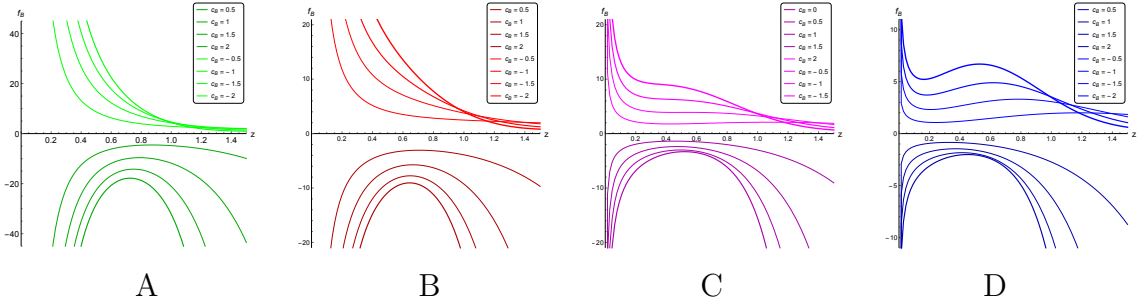


Figure 4. Coupling function $f_B(z)$ for different c_B for $\nu = 1$ (A), $\nu = 1.5$ (B), $\nu = 3$ (C), $\nu = 4.5$ (D); $c = 0.227$, $z_h = 1$, $\mu = 0$, $q_B = 1$.

Comparing Fig.1.A-D one can notice, that the primary QGP anisotropy, parametrized by ν , suppresses the external magnetic field influence on the blackening function. Moreover, this suppression isn't equal for positive and negative values of coupling coefficient c_B . For $\nu = 4.5$ (Fig.1.D) difference between $c_B = 0$ and $c_B = 0.5$ is the smallest comparing to the lesser anisotropy cases (Fig.1.A-C), while curves for $c_B = 1.5$ and $c_B = 2$ can be hardly distinguished from each other.

On Fig.2 blackening function depending on chemical potential for $c_B = -1$ and primary anisotropy ($1 \leq \nu \leq 4.5$) is plotted. One can see that the presence of magnetic field doesn't change the picture in general: increasing chemical potential still leads to decreasing of the blackening function values and to the shrinkage of the black hole horizon value as it was in [28]. Increase of primary anisotropy (larger ν values) enhances the effect of the chemical potential on the blackening function behavior.

On Fig.3 blackening function dependence on μ for different c_B is compared. For larger absolute value of c_B chemical potential demonstrates weaker effect of blackening function for small z , but stronger influence on the horizon position. In the absence of primary anisotropy ($\nu = 1$ on Fig.3.A) this influence on the horizon position is the most obvious.

Coupling function f_B (2.18) depends both on the coefficient c_B and the magnetic

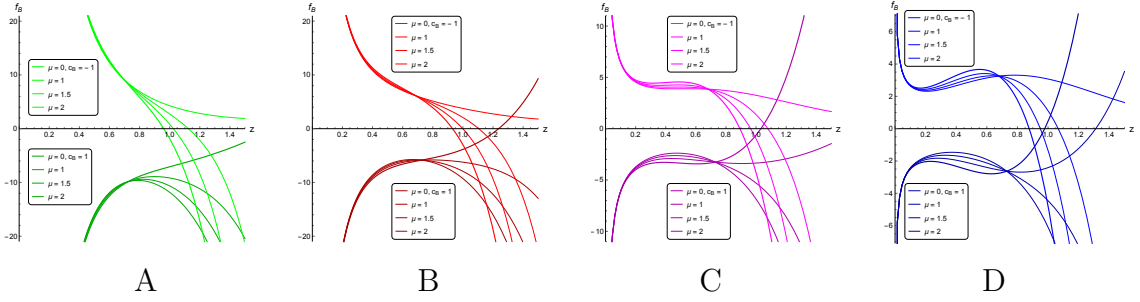


Figure 5. Coupling function $f_B(z)$ for different μ for $\nu = 1$ (A), $\nu = 1.5$ (B), $\nu = 3$ (C), $\nu = 4.5$ (D); $c = 0.227$, $z_h = 1$, $c_B = \pm 1$, $q_B = 1$.

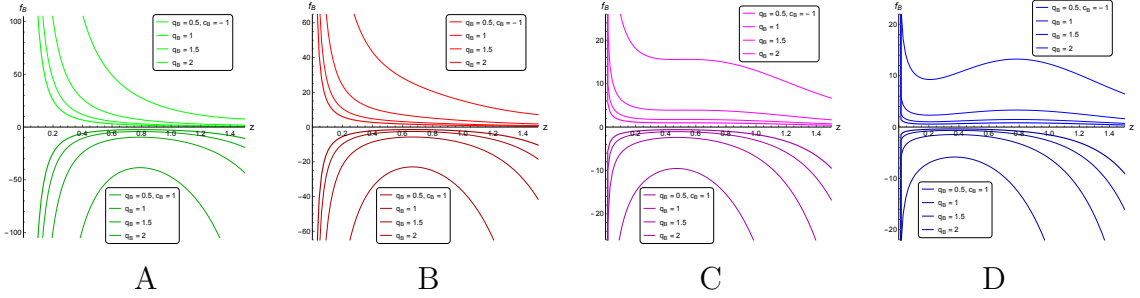


Figure 6. Coupling function $f_B(z)$ for different q_B for $\nu = 1$ (A), $\nu = 1.5$ (B), $\nu = 3$ (C), $\nu = 4.5$ (D); $c = 0.227$, $z_h = 1$, $\mu = 0$, $c_B = \pm 1$.

“charge” q_B . First of all, f_B behavior forces us to limit ourselves to $c_B < 0$ only, as $c_B > 0$ makes f_B take negative values above the horizon ($z < z_h$) thus violating the NEC (Fig.4). For $\nu = 1, 1.5$ (Fig.4.A,B) f_B decreases monotonically. Larger primary anisotropy (Fig.4.C,D for $\nu = 3, 4.5$) leads to more complex function behavior and even to the appearance of local maximum (Fig.4.D). This effect is more significant for the larger absolute values of c_B .

Increasing chemical potential makes the coupling function f_B with $c_B < 0$ decrease faster (Fig.5) and reach negative values earlier. Does it mean that large chemical potential forces f_B to break NEC at the outer vicinity of horizon? Not really. We should not forget that the horizon itself shifts to smaller z_h values because of large chemical potentials. Let us make sure that point, where f_B reaches zero, lies inside of horizon anyway as $f_B(z_h)$ is still positive.

According to our boundary condition (2.13) $g(z_h) = 0$. Therefore expression (2.18) can be simplified as

$$f_B(z_h) = 2 \left(\frac{z}{L} \right)^{-\frac{2}{\nu}} e^{-\frac{1}{2}c_B z^2} \frac{c_B z}{q_B^2} g'(z_h) > 0, \quad (2.22)$$

At first horizon (the one that really matters) blackening function is decreasing, so $g'(z_h) < 0$. If we also take $c_B < 0$, their product is positive, all the other multipliers

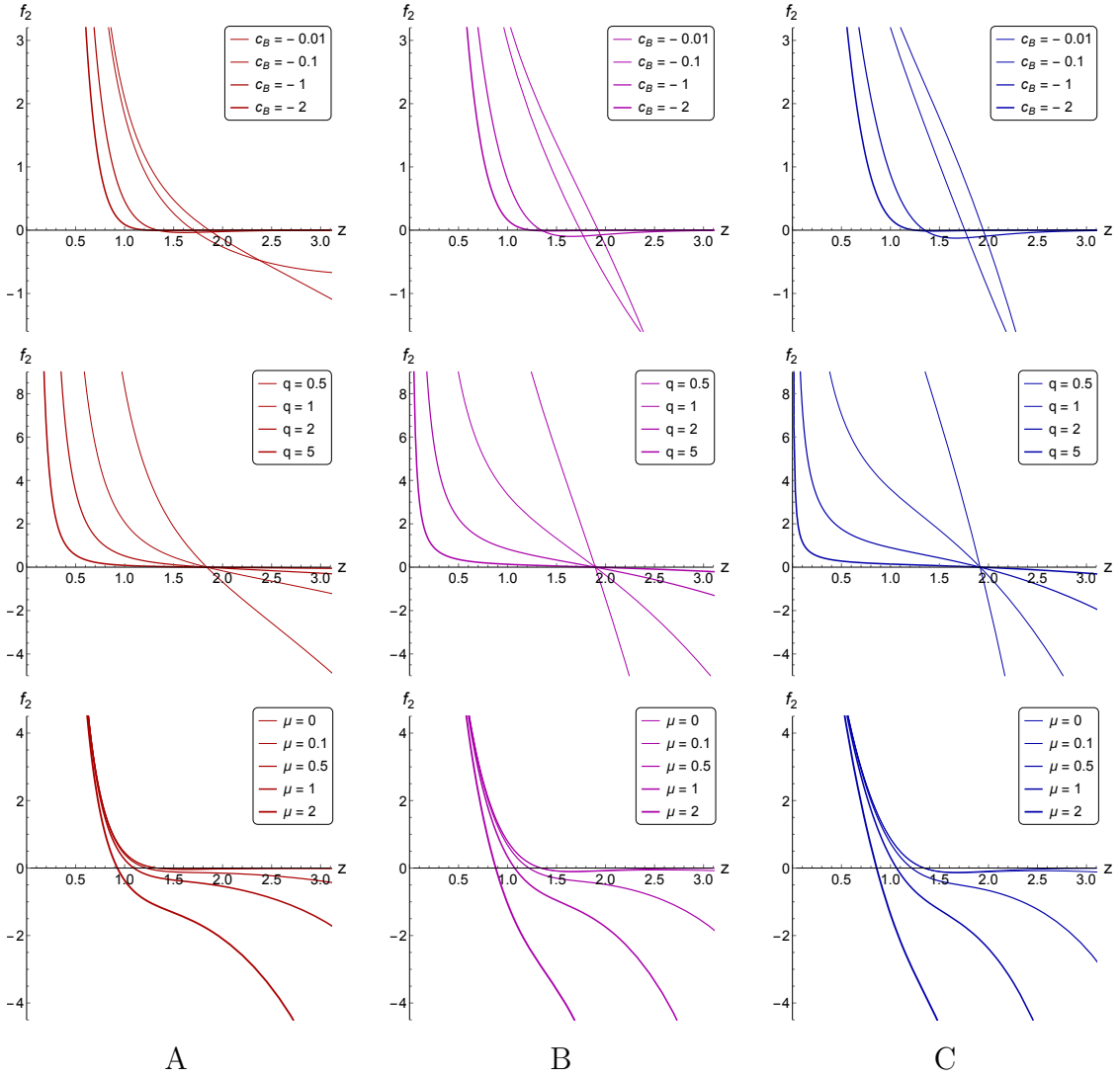


Figure 7. Coupling function $f_2(z)$ for different c_B , $\mu = 0$, $q = 1$ (first line), for different q $\mu = 0$, $c_B = -1$ (second line), for different μ , $c_B = -1$, $q = 1$ (third line) in anisotropic cases for $\nu = 1.5$ (A), $\nu = 3$ (B), $\nu = 4.5$ (C); $c = 0.227$, $z_h = 1$.

in (2.22) are positive as well, therefore $f_B(z_h) > 0$ for any negative c_B in the z_h interval we need.

Until now we only spoke about dependences on c_B , that characterizes the connection between metric and the external magnetic field, but told nothing about the strength of that magnetic field itself. This quality is described by “charge” q_B .

From (2.18) we see that the coupling function f_B depends on the inverse square of the “charge” q_B . So the larger q_B is, the faster f_B tends to zero and the longer is in its vicinity (Fig.6).

Let us remind that, unlike the third Maxwell $F_{\mu\nu}^{(B)}$, the second Maxwell field $F_{\mu\nu}^{(2)}$ isn’t physical and serves to maintain primary anisotropy, set by parameter ν , of the

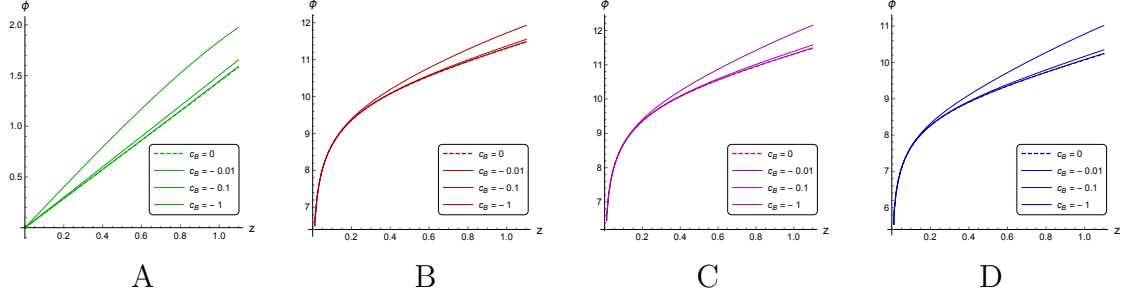


Figure 8. Coupling function $f_B(z)$ for different c_B for $\nu = 1$ (A), $\nu = 1.5$ (B), $\nu = 3$ (C), $\nu = 4.5$ (D); $c = 0.227$, $z_h = 1$, $\mu = 0$.

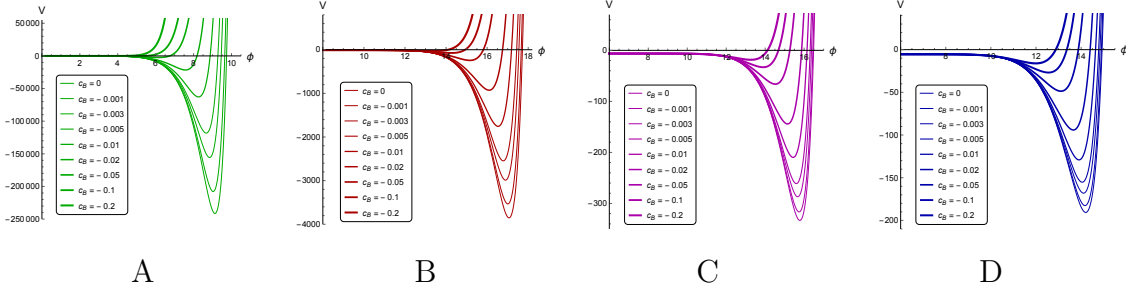


Figure 9. Scalar potential $V(\phi)$ for different c_B for $\nu = 1$ (A), $\nu = 1.5$ (B), $\nu = 3$ (C), $\nu = 4.5$ (D); $c = 0.227$, $z_h = 1$, $\mu = 0$.

black hole solution within the holographic approach.

Behavior of the coupling function f_2 (2.19) in this model is quite similar to its behavior in the absence of external magnetic field [28] (Fig.7). Mainly this function decreases monotonically, larger chemical potentials and larger q – “charges” of $F_{\mu\nu}^{(2)}$ – provide faster decrease. These effects are more obvious for larger ν . Case $\nu = 1$ doesn’t make sense, as $F_{\mu\nu}^{(2)} \equiv 0$ and its coupling function f_2 do not exist.

For rather large absolute values of coefficient c_B (for example $c_B = -1$) function f_2 has local minimum, that is more obvious for larger primary anisotropy (Fig.7.C). But this effect is suppressed by chemical potential.

We can show that f_2 doesn’t break NEC above the horizon like it was done for f_B earlier:

$$f_2(z_h) = 4 \left(\frac{z}{L} \right)^{2-\frac{4}{\nu}} e^{-\frac{1}{2}(c-2c_B)z^2} \frac{\nu-1}{q^2\nu z} (-g'). \quad (2.23)$$

At first horizon $g(z_h) = 0$ and $g'(z_h) < 0$. As f_2 has sense for $\nu > 1$ only, all the multipliers in (2.23) are positive, so $f_2(z_h) > 0$ and NEC isn’t broken so far.

Unlike our previous light quarks model [44], this time $z_0 = 0$ is restricted even for $\nu = 1$. But we can take z_0 small enough to maintain the connection to the isotropic limit [19].

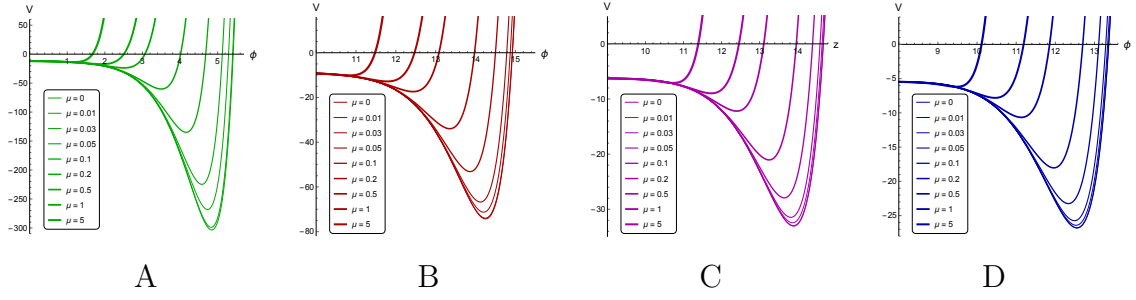


Figure 10. Scalar potential $V(\phi)$ for different μ for $\nu = 1$ (A), $\nu = 1.5$ (B), $\nu = 3$ (C), $\nu = 4.5$ (D); $c = 0.227$, $z_h = 1$, $c_B = -0.1$.

Scalar field doesn't depend on q_B that characterizes the external magnetic field $F_{\mu\nu}^{(B)}$. Dependence on the coupling coefficient c_B is rather slight and weakens with the rise of primary anisotropy, parametrized by ν (Fig.8).

The effect of increasing c_B absolute value on $V(\phi)$ (Fig.9) is similar to increasing chemical potential (Fig.10): local minimum becomes larger and its position shifts to the left. Case $\nu = 1$ still differs from the others, as $V(\phi_{min} = 0) = 0$. For larger ν we can say that if $\nu_1 < \nu_2$, therefore $V(0)|_{\nu_1} < V(0)|_{\nu_2}$, $V_{min}|_{\nu_1} < V_{min}|_{\nu_2}$ and for $\phi_* : V(\phi) = V_{min}$ we have $\phi_*|_{\nu_1} > \phi_*|_{\nu_2}$, but $\phi_*|_{\nu \neq 1} > \phi_*|_{\nu=1}$. For larger primary anisotropy ν influence of both c_B and μ weakens.

3 Thermodynamics

3.1 Temperature and entropy

For the metric (2.3) and the warp-factor $f_{1HQ} = z^{-2+\frac{2}{\nu}}$ (2.15) temperature and entropy can be written as:

$$\begin{aligned}
T &= \left. \frac{|g'|}{4\pi} \right|_{z=z_h} = \frac{1}{2\pi} \left| -e^{\frac{1}{4}(3c-2c_B)z_h^2} (2c_B - c) z_h^{1+\frac{2}{\nu}} \left\{ \frac{\mu^2 e^{\frac{1}{4}(c-2c_B)z_h^2}}{4L^2 \left(1 - e^{\frac{1}{4}(c-2c_B)z_h^2}\right)^2} + \right. \right. \\
&+ \left. \left. \left(\frac{3}{4}\right)^{1+\frac{1}{\nu}} \frac{(2c_B - c)^{\frac{1}{\nu}}}{\Gamma\left(1 + \frac{1}{\nu}; 0\right) - \Gamma\left(1 + \frac{1}{\nu}; \frac{3}{4}(2c_B - c)z_h^2\right)} \right\} \times \right. \\
&\times \left. \left[1 - \frac{\mu^2 (2c_B - c)^{-\frac{1}{\nu}}}{4L^2 \left(1 - e^{\frac{1}{4}(c-2c_B)z_h^2}\right)^2} \left(\Gamma\left(1 + \frac{1}{\nu}; 0\right) - \Gamma\left(1 + \frac{1}{\nu}; (2c_B - c)z_h^2\right) \right) \right] \right|, \\
s &= \frac{1}{4} \left(\frac{L}{z_h} \right)^{1+\frac{2}{\nu}} e^{-\frac{1}{4}(3c-2c_B)z_h^2}. \tag{3.2}
\end{aligned}$$

On Fig.11 we see, that temperature is quite sensible to c_B even for zero chemical potential. Function $T(z_h)$ is multivalued for $c_B > -0.02 \div -0.01$ (for different ν). For larger anisotropy the ambiguity of temperature is preserved till larger absolute value of coupling coefficient c_B .

Temperature dependence on chemical potential in the presence of external magnetic field is similar to the previous model [28] (Fig.12). For larger anisotropy the ambiguity of temperature is preserved for larger μ values: till $\mu \approx 0.05$ for $\nu = 1$ (Fig.12.A) vs $\mu \approx 0.3$ for $\nu = 4.5$ (Fig.12.D).

Behavior of entropy as function of temperature for different values of the coupling coefficient c_B (Fig.13) and chemical potential μ (Fig.14) convinces us of the conclusions drawn above. Therefore the confinement/deconfinement phase transition provided by the background (that we called a Hawking-Page-like phase transition previously [28, 30, 44, 52]) in the presence of magnetic field significantly depends on the coupling coefficient c_B . If the connection of metric with the external magnetic field is too strong ($c_B < -0.02 \div -0.01$ for different ν), the background phase transition shouldn't happen at all. Note, that this process doesn't generally depend on the strength of the field $F_{\mu\nu}^{(B)}$ itself, as both temperature and entropy functions do not contain "charge" q_B explicitly. So the coupling coefficient c_B turns out to be the parameter that can be fitted via background phase transition.

To ensure that BH-BH transition caused by three-valued temperature function is a phase transition let us consider density ρ , that is a coefficient in A_t expansion:

$$A_t = \mu - \rho z^2 + \dots = \mu + \frac{(c - 2c_B) \mu z^2}{4 \left(1 - e^{\frac{1}{4}(c-2c_B)z_h^2}\right)} + \dots, \quad (3.3)$$

$$\rho = - \frac{(c - 2c_B) \mu}{4 \left(1 - e^{\frac{1}{4}(c-2c_B)z_h^2}\right)}. \quad (3.4)$$

On Fig.15 ρ/μ ratio as a function of temperature for primary isotropic solution ($\nu = 1$, Fig.15.A) and anisotropic solution ($\nu = 4.5$, Fig.15.B) are plotted. Vertical

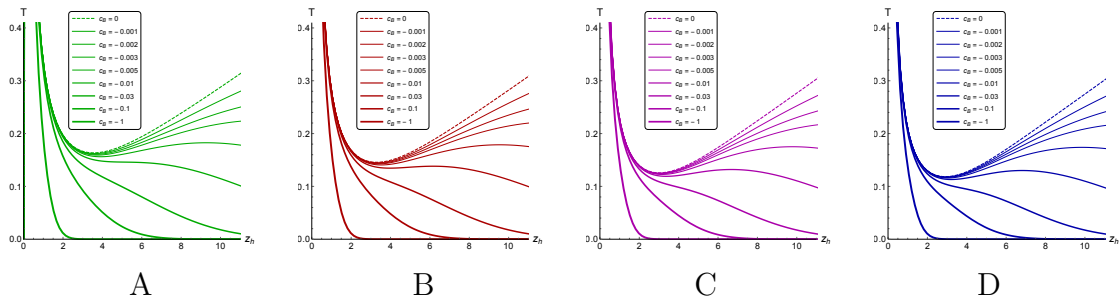


Figure 11. Temperature $T(z_h)$ for different c_B for $\nu = 1$ (A), $\nu = 1.5$ (B), $\nu = 3$ (C), $\nu = 4.5$ (D); $c = 0.227$, $\mu = 0$.

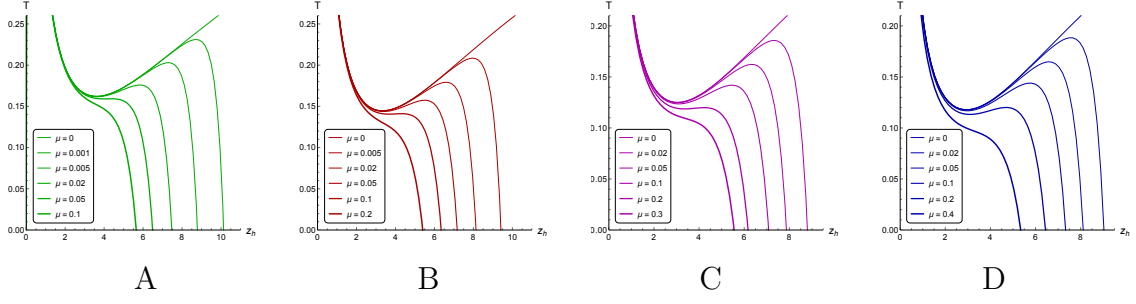


Figure 12. Temperature $T(z_h)$ for different μ for $\nu = 1$ (A), $\nu = 1.5$ (B), $\nu = 3$ (C), $\nu = 4.5$ (D); $c = 0.227$, $c_B = -0.001$.

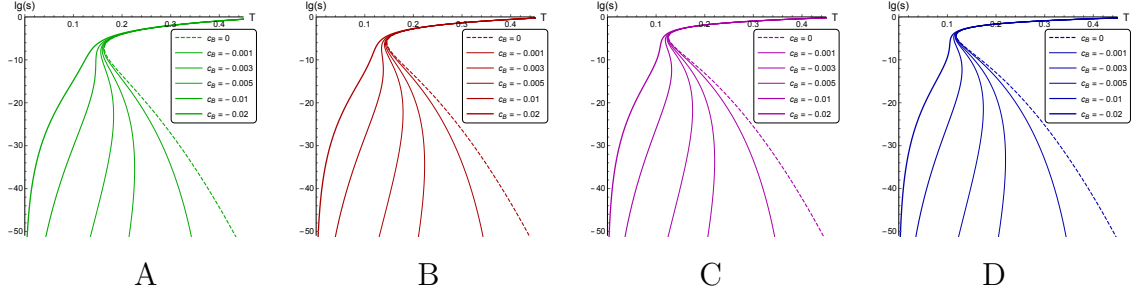


Figure 13. Entropy $s(T)$ (in logarithmic scale) for different c_B for $\nu = 1$ (A), $\nu = 1.5$ (B), $\nu = 3$ (C), $\nu = 4.5$ (D); $c = 0.227$, $\mu = 0$.

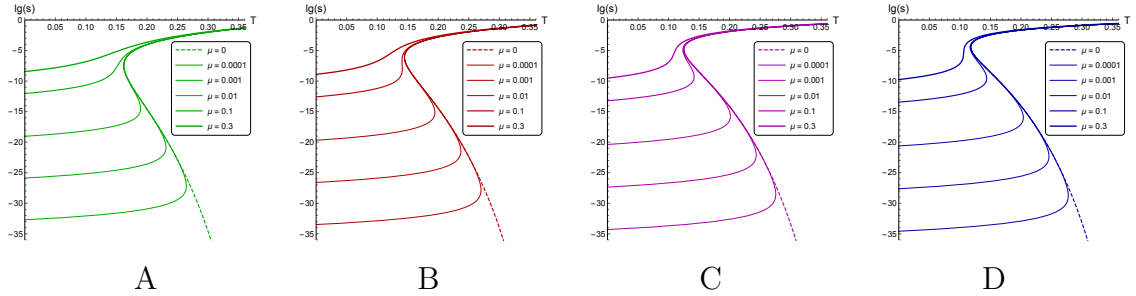


Figure 14. Entropy $s(T)$ (in logarithmic scale) for different μ for $\nu = 1$ (A), $\nu = 1.5$ (B), $\nu = 3$ (C), $\nu = 4.5$ (D); $c = 0.227$, $z_h = 1$, $c_B = -0.001$.

arrows show the BH-BH transition direction. Function ρ/μ is a three-digit function of T as expected, and we can see that collapse from small black holes (larger z_h) to the large ones (smaller z_h) is accompanied by a sharp rise of the density for any appropriate chemical potential. On Fig.15 $c_B = 0$, but for c_B close to zero enough to preserve ambiguity of $T(z_h)$ -function density curves will differ from the zero magnetic field case negligibly.

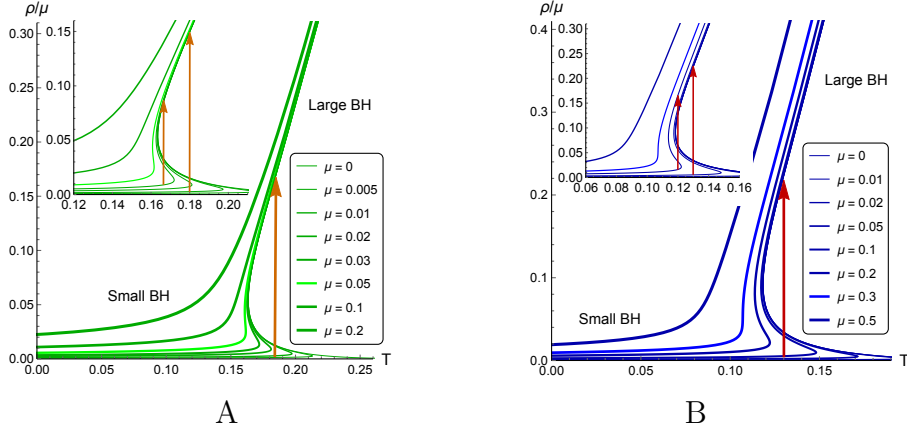


Figure 15. Density $\rho/\mu(T)$ for different μ for $\nu = 1$ (A) and $\nu = 4.5$ (B); $c = 0.227$, $c_B = 0$.

3.2 Free energy and background phase transition

To get BH-BH phase transition, that originates from the model background, we need to consider the free energy as a function of temperature:

$$F = \int_{z_h}^{\infty} s T' dz, \quad dF = s T'. \quad (3.5)$$

Using free energy we can estimate the lifetime of the unstable state. For the general case we should include the free energy of the black hole F_{BH} and the free energy of the quarks pair $F_{q\bar{q}}$ into consideration and also take both connected and disconnected string configurations into account. Therefore the total free energy characterizing our system is $F_{tot} = F_{q\bar{q}} + F_{BH}$. However for small distance ℓ between quarks the difference of free energy values between connected and disconnected string configurations $\Delta F_{q\bar{q}}$ is small [19, 34]. For small ℓ we assume $\Delta F_{q\bar{q}} \ll \Delta F_{BH}$. Therefore the total free energy difference between configurations is $\Delta F_{tot} = \Delta F_{q\bar{q}} + \Delta F_{BH} \approx \Delta F_{BH}$. In this case the lifetime of the unstable state can be estimated as:

$$\tau = \frac{\hbar}{\Delta F_{tot}(T, \mu)} = \frac{\hbar}{\Delta F_{BH}(T, \mu)}. \quad (3.6)$$

On Fig.16 an example of such an estimation is illustrated. Vertical lines show the chosen temperature $T = 0.164$ (Fig.16.A,B) or $T = 0.122$ (Fig.16.C). It is orange for $\nu = 1$ (Fig.16.A) and red for $\nu = 4.5$ (Fig.16.B,C).

In the absence of magnetic field the free energy difference between two states of the transition is the distance between two red points located on the orange temperature vertical for $\nu = 1$ (Fig.16.A) and between two magenta points located on the red temperature vertical for $\nu = 4.5$ (Fig.16.B,C). For $c_B = -0.001$ the free energy difference is the distance between two dark red points on the same temperature verticals. But on scale of Fig.16.B curves for $c_B = 0$ and $c_B = -0.001$ almost coincide, so red and magenta points merge on this plot.

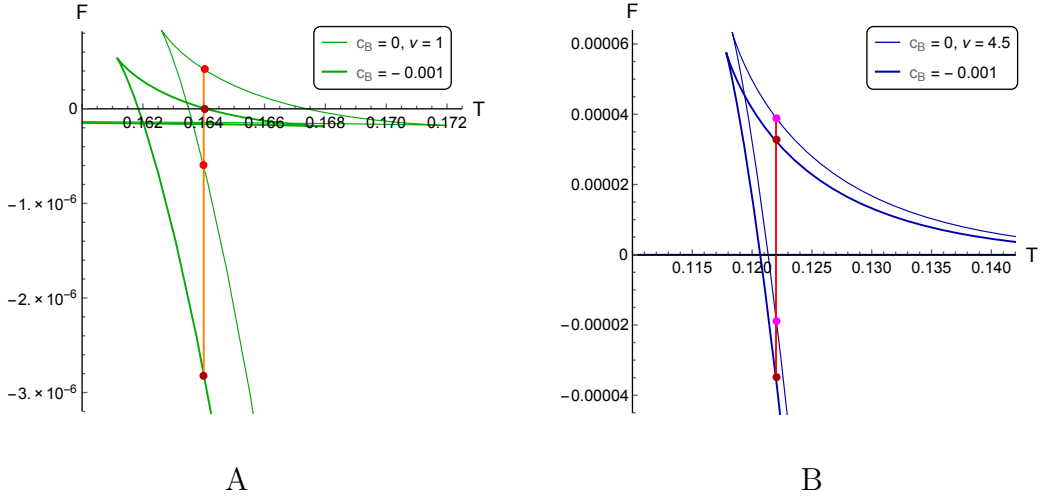


Figure 16. Free energy difference $\Delta F(T)$ for $c_B = 0$ and $c_B = -0.001$, $\nu = 1$ (A) and $\nu = 4.5$ (B); $c = 0.227$, $\mu = 0.03$ and $T = 0.164$.

Taking the coordinates of all these points we have

$$\begin{aligned}
 \tau \Big|_{\nu=1, \mu=0.03, T=0.164, c_B=0} &= \frac{\hbar}{4.2 \cdot 10^{-7} - (-6.131 \cdot 10^{-7})} \approx 6.39 \cdot 10^{-19} \text{ s}, \\
 \tau \Big|_{\nu=1, \mu=0.03, T=0.164, c_B=-0.001} &= \frac{\hbar}{1.314 \cdot 10^{-8} - (-2.807 \cdot 10^{-6})} \approx 2.34 \cdot 10^{-19} \text{ s}, \\
 \tau \Big|_{\nu=4.5, \mu=0.03, T=0.122, c_B=0, -0.001} &= \frac{\hbar}{3.469 \cdot 10^{-6} - (-3.132 \cdot 10^{-3})} \approx 2.10 \cdot 10^{-22} \text{ s}, \\
 \tau \Big|_{\nu=4.5, \mu=0.03, T=0.122, c_B=0} &= \frac{\hbar}{3.92 \cdot 10^{-5} - (-1.81 \cdot 10^{-5})} \approx 1.15 \cdot 10^{-20} \text{ s}, \\
 \tau \Big|_{\nu=4.5, \mu=0.03, T=0.122, c_B=-0.001} &= \frac{\hbar}{3.264 \cdot 10^{-5} - (-3.413 \cdot 10^{-5})} \approx 9.88 \cdot 10^{-21} \text{ s}.
 \end{aligned} \tag{3.7}$$

Therefore the lifetime of the unstable state is about 10^{-22} – 10^{-19} s, that is larger than the lifetime of QGP. For $\nu = 1$ presence of magnetic field decreases this value in about 2.7 times, while for $\nu = 4.5$ – in less than 1.2 times. So the external magnetic field generally reduces the lifetime of an unstable state, but primary anisotropy $\nu > 1$ weakens this effect.

On Fig.17 BH-BH transition lines for different values of primary and secondary anisotropy are presented. Fig.17.A-D display families of curves representing BH-BH phase transition lines for different values of primary anisotropy parameter, i.e. Fig.17.A for $\nu = 1$, Fig.17.B for $\nu = 1.5$, Fig.17.C for $\nu = 3$ and Fig.17.D for $\nu = 4.5$.

First of all, larger absolute values of the coupling coefficient c_B lead to decrease of the transition temperature, so the effect of the inverse magnetic catalysis takes

place. Besides, the length of the Hawking-Page line also decreases and eventually degenerates. However primary anisotropy weakens these effects, so BH-BH phase transition is preserved for larger absolute values of the coupling coefficient. For example, background phase transition still exists for $c_B = -0.018$ and $\nu = 4.5$ (Fig.17.D), whereas for $c_B = -0.001$ and $\nu = 1$ no such curve can be plotted (Fig.17.A).

On Fig.17.E all the BH-BH phase transition lines are combined into one plot. One can see, that the distance between lines for the same pairs of c_B values shrinks for larger ν , while their length along the μ -axis, on the contrary, grows. Both anisotropy parameters ν and c_B lower the transition temperature, but other their effects on the background phase transition picture can be considered the opposite.

We can also consider positions of the “free ends” of the BH-BH phase transition lines (let us call it “critical end-points for heavy quarks”, CEP_{HQ}). On Fig.18 these positions are depicted on $T-\mu$ (Fig.18.A), $\mu-c_B$ (Fig.18.B) and $T-c_B$ (Fig.18.C) planes. For $\nu = 1$ temperature of the CEP_{HQ} falls relatively quickly with the c_B absolute value growth, while for $\nu = 4.5$ this temperature is almost constant (Fig.18.A,C). On the contrary, chemical potential of the CEP_{HQ} -points falls more for larger primary anisotropy, especially quickly decreasing near the $\mu = 0$. On Fig.19 the 3D-plots for the CEP_{HQ} positions depending on coupling coefficient c_B , chemical potential and temperature for different values of primary anisotropy are displayed.

3.3 Temporal Wilson loops

To calculate the expectation value of the temporal Wilson loop

$$W[C_\vartheta] = e^{-S_{\vartheta,t}}, \quad (3.8)$$

oriented along vector \vec{n} :

$$n_{x1} = \cos \vartheta \sin \alpha, \quad n_{x2} = \sin \vartheta \sin \alpha, \quad n_{x3} = \cos \alpha \quad (3.9)$$

we use our metric (2.3) as a background:

$$ds^2 = G_{\mu\nu} dx^\mu dx^\nu = \frac{L^2}{z^2} \mathfrak{b}_s(z) \left[-g(z) dt^2 + \mathfrak{g}_1 dx^2 + \mathfrak{g}_2 dy_1^2 + \mathfrak{g}_3 dy_2^2 + \frac{dz^2}{g(z)} \right], \quad (3.10)$$

Following the holographic approach we calculate the value of the Nambu-Goto action for test string in our background in string frame:

$$S = \frac{1}{2\pi\alpha'} \int d\xi^0 d\xi^1 \sqrt{-\det h_{\alpha\beta}}, \quad h_{\alpha\beta} = G_{\mu\nu} \partial_\alpha X^\mu \partial_\beta X^\nu. \quad (3.11)$$

The world sheet is parameterized as (Fig.20)

$$\begin{aligned} X^0 \equiv t &= \xi^0, & X^1 \equiv x &= \xi^1 \cos \vartheta \sin \alpha, & X^2 \equiv y_1 &= \xi^1 \sin \vartheta \sin \alpha, \\ X^3 \equiv y_2 &= \xi^1 \cos \alpha, & X^4 \equiv z &= z(\xi^1). \end{aligned} \quad (3.12)$$

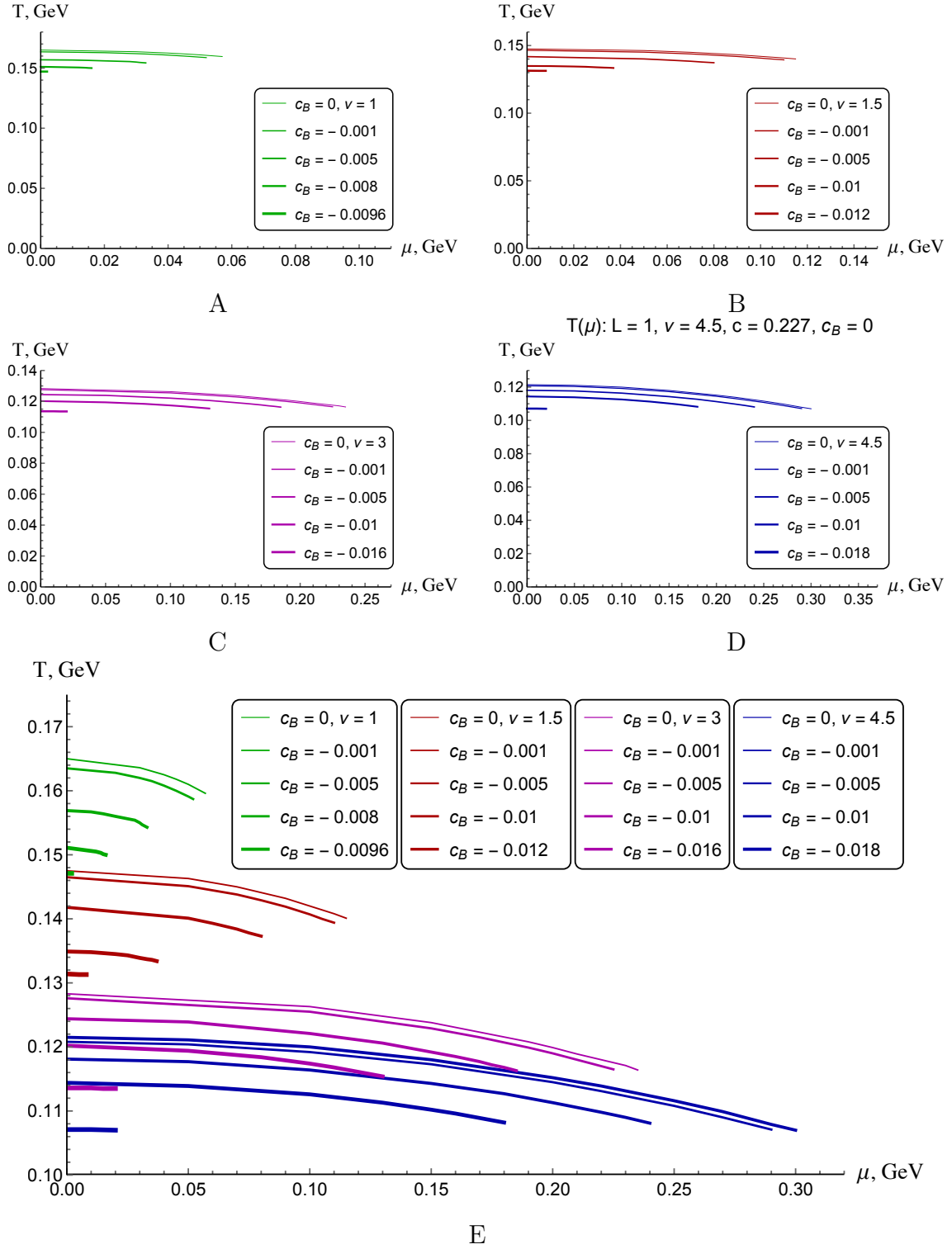


Figure 17. Background phase transition lines depending on c_B for $\nu = 1$ (A), $\nu = 1.5$ (B), $\nu = 3$ (C), $\nu = 4.5$ (D) and all of them together (E); $c = 0.227$.

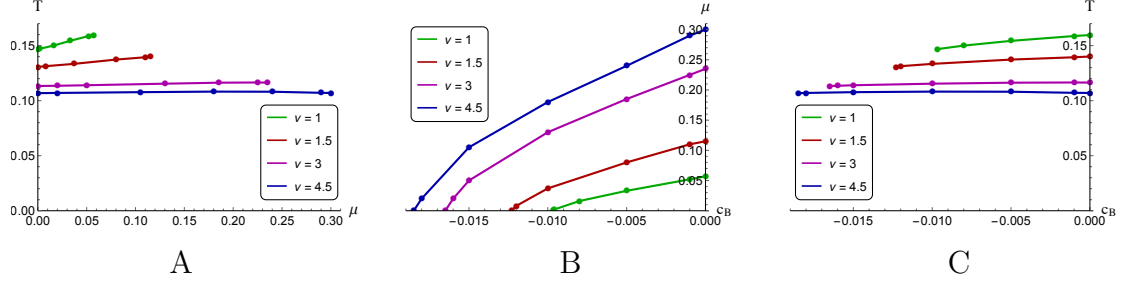


Figure 18. Position of critical end-points CEP_{HQ} for heavy quarks model depending on μ and T (A), c_B and μ (B), c_B and T (C) for $\nu = 1, 1.5, 3, 4.5$, $c = 0.227$.

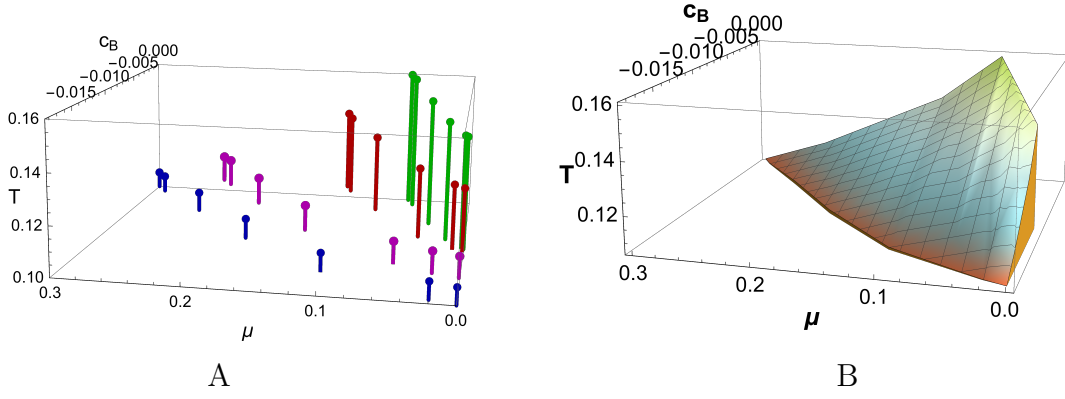


Figure 19. Temperature of critical end-points CEP_{HQ} for heavy quarks model depending on c_B and μ for $1 \leq \nu \leq 4.5$ as a set of point (A) and as a 3D-surface (B), $c = 0.227$.

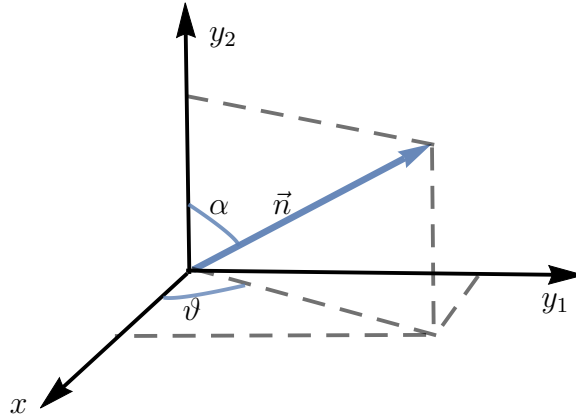


Figure 20. World sheet parametrization for the Wilson loop orientation vector \vec{n} .

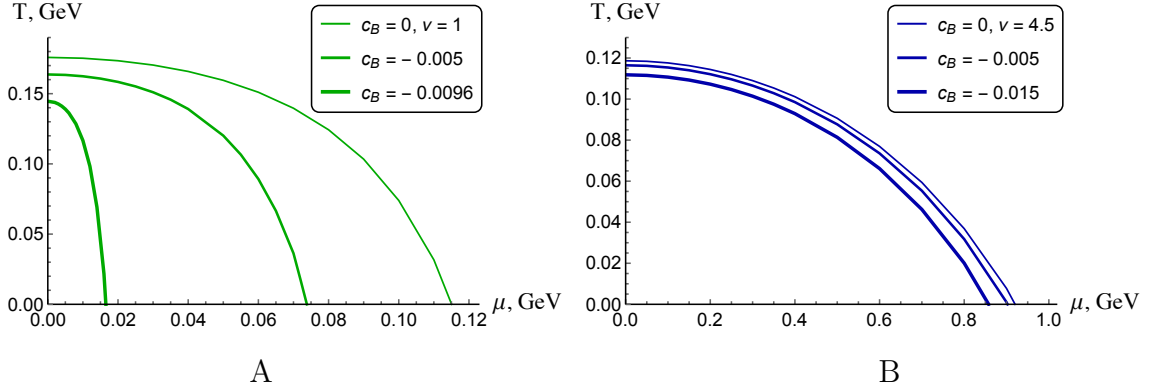


Figure 21. Wilson loop transition lines for different c_B for $\nu = 1$ (A) and $\nu = 4.5$ (B); $c = 0.227$.

Let us denote $\xi \equiv \xi^1$, rewrite Nambu-Goto action (3.11)

$$\begin{aligned}
 S &= -\frac{\tau}{2\pi\alpha'} \int d\xi M(z(\xi)) \sqrt{\mathcal{F}(z(\xi)) + (z'(\xi))^2}, \quad \tau = \int d\xi^0, \\
 M(z(\xi)) &= \frac{\mathbf{b}_s(z(\xi))}{z^2(\xi)}, \\
 \mathcal{F}(z(\xi)) &= g(z(\xi^1)) (\mathbf{g}_1 \cos^2 \vartheta \sin^2 \alpha + \mathbf{g}_2 \sin^2 \vartheta \sin^2 \alpha + \mathbf{g}_3 \cos^2 \alpha)
 \end{aligned} \tag{3.13}$$

and introduce the effective “potential”

$$\begin{aligned}
 \mathcal{V}(z(\xi)) &\equiv M(z(\xi)) \sqrt{\mathcal{F}(z(\xi))} = \\
 &= \frac{\mathbf{b}_s(z(\xi))}{(z^2(\xi))} \sqrt{g(z(\xi)) (\mathbf{g}_1 \cos^2 \vartheta \sin^2 \alpha + \mathbf{g}_2 \sin^2 \vartheta \sin^2 \alpha + \mathbf{g}_3 \cos^2 \alpha)}.
 \end{aligned} \tag{3.14}$$

Thus for the current heavy quarks model Wilson loops, oriented along x , y_1 and y_2 axes, are defined:

$$\begin{aligned}
 \mathcal{D}\mathcal{W}_x &\equiv -cz + \sqrt{\frac{2}{3}} \phi'(z) + \frac{g'}{2g} - \frac{2}{z} \Big|_{z=z_{DWx}} = 0, \\
 \mathcal{D}\mathcal{W}_{y_1} &\equiv -cz + \sqrt{\frac{2}{3}} \phi'(z) + \frac{g'}{2g} - \frac{\nu+1}{\nu z} \Big|_{z=z_{DWy_1}} = 0, \\
 \mathcal{D}\mathcal{W}_{y_2} &\equiv -cz + \sqrt{\frac{2}{3}} \phi'(z) + \frac{g'}{2g} - \frac{\nu+1}{\nu z} + c_B z \Big|_{z=z_{DWy_2}} = 0.
 \end{aligned} \tag{3.15}$$

It is obvious, that for $c_B = 0$ expressions in (3.15) for y_1 and y_2 become equal, and putting $\nu = 1$ leaves the x -expression only. Behaviour of \mathcal{W}_x and \mathcal{W}_{y_1} was already considered [28, 30].

On Fig.21 curves for $c_B = 0$ can also be considered to represent \mathcal{W}_{y_1} transition lines. We see, that the appearance of external magnetic field ($c_B \neq 0$) makes the

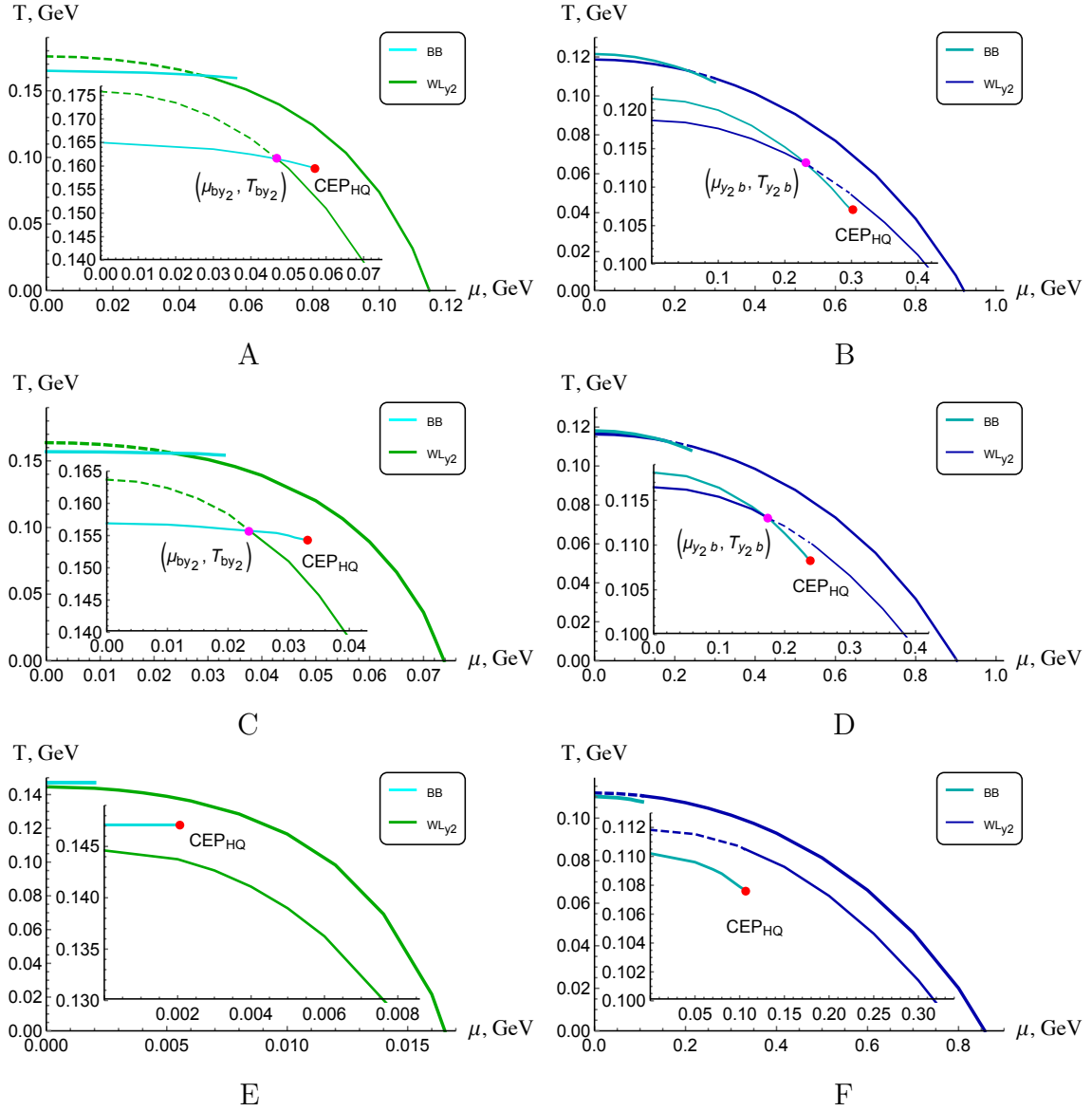


Figure 22. Phase diagram for y_2 -orientation for $c_B = 0$, $\nu = 1$ (A) and $\nu = 4.5$ (B), $c_B = -0.005$, $\nu = 1$ (C) and $\nu = 4.5$ (D), $c_B = -0.0096$, $\nu = 1$ (E) and $c_B = -0.015$, $\nu = 4.5$ (F); $c = 0.227$.

Wilson loop phase transition line to shrink. For $\nu = 1$ maximum chemical potential at $T = 0$ decreases faster than maximum temperature at $\mu = 0$. For $\nu = 4.5$ the shrinkage of the phase transition line corresponding to y_2 Wilson loop is much weaker and looks almost cocentric.

On Fig.22 phase transition diagrams for y_2 -oriented Wilson loops are displayed. We see the picture quite similar to our previous results for heavy quarks.

For $\nu = 1$ without magnetic field (Fig.22.A) BH-BH line determines the confinement/deconfinement phase transition for $0 \leq \mu \leq \mu_{by_2} = 0.04666$ till the intersection

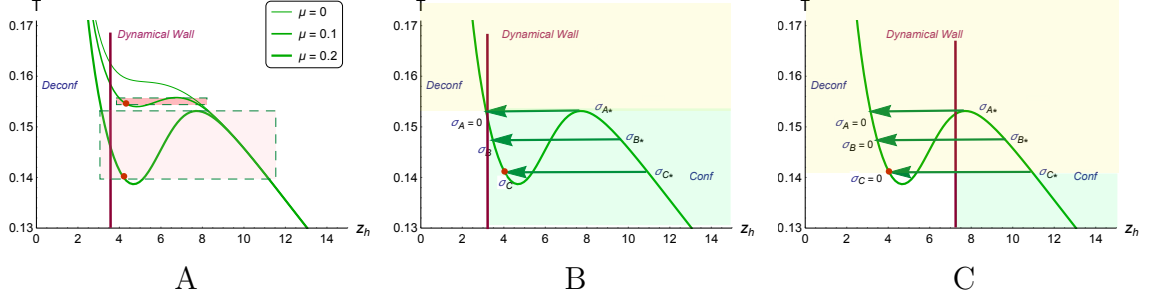


Figure 23. Scheme of confinement/deconfinement depending on location of the BH-BH phase transition points relative to the dynamic wall.

with the y_2 Wilson loop line at point $(0.04666; 0.1617)$.

If we turn on the external magnetic field, the intersection between BH-BH line and Wilson loop line shifts to smaller temperature and chemical potential, $(0.0235; 0.1558)$ for $c_B = -0.005$ (Fig.22.C), and the total area of confinement phase predictably decreases. Also phase transition lines, corresponding to the background (BH-BH) and string action (WLy_2), become closer to each other.

When the coupling with the $F_{\mu\nu}^{(B)}$ is almost maximum ($c_B = -0.0096$), BH-BH transition line turns out to be above the y_2 Wilson loop line without any intersection (Fig.22.E).

For $\nu = 4.5$ the picture can be called the opposite from some point of view. Without the external magnetic field (Fig.22.B) y_2 Wilson loop line plays the main role for $\mu \leq \mu_{y_2b} = 0.2448$ till the intersection with the BH-BH line at $(0.2448; 0.1121)$. BH-BH phase transition line lasts till the CEP_{HQ} at $(0.3; 0.107)$, where the main role comes back to Wilson loop line via the jump to higher temperature.

For $c_B = -0.005$ the picture remains the same qualitatively (Fig.22.D). Transition lines intersect at point $(0.1753; 0.113)$, i.e. at lesser chemical potential, but a little higher temperature.

Eventually BH-BH transition line turns out to lie entirely under the WL-line till $(0.24, 0.1081)$, where it's CEP is located (Fig.22.F). Critical value of the coupling function, for which $T_{BH-BH}|_{\mu=0} = T_{WLy_2}|_{\mu=0}$ is about $c_{B\text{crit}} \approx -0.11$ in this case.

In the backgrounds with instability one has also to check that the extended surface lies in the stability zone [50]. This allows to determine roles of different transition lines in the general confinement/deconfinement picture.

There are different situations in this matter. For given μ the dynamic wall (DW) can be out of instability zone (small rectangular pink region on Fig.23.A), or cross the instability zone starting from some temperature (large rectangular pink region on Fig.23.A). In the first case the jump to the stable zone keeps confinement, the string tension decreases from σ_* to σ , $\sigma_* > \sigma$ and we land in the stable phase, that can be interpreted as quarkyonic (Fig.23.B). If the DW lies in unstable zone we lose the linear interaction between quarks in the quarkyonic phase (Fig.23.C).

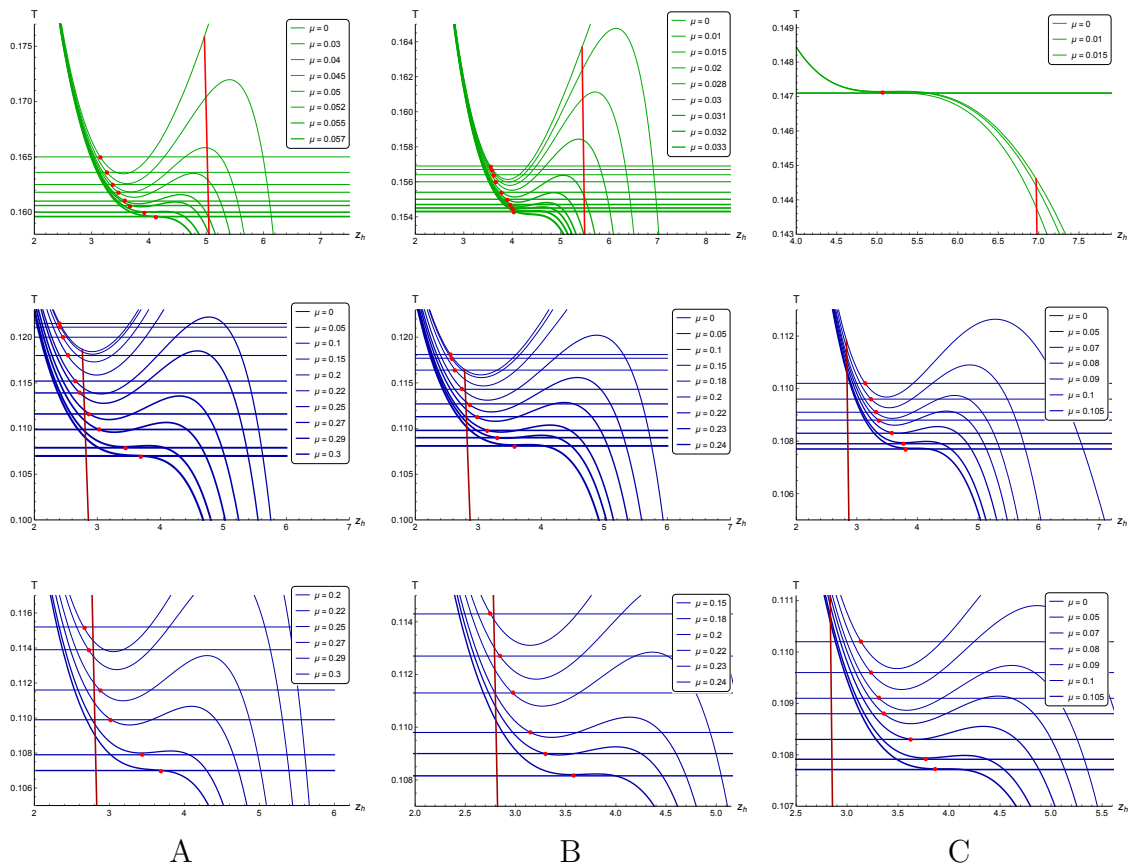


Figure 24. Location of the BH-BH phase transition points (red point) relative to the dynamic wall (red lines) for $\nu = 1$ (first line) and $\nu = 4.5$ (second and third line, third line is the zoom of the second) for $c_B = 0$ (A), $c_B = -0.005$ (B), $c_B = -0.0096$ for $\nu = 1$ and $c_B = -0.015$ for $\nu = 4.5$, $c = 0.227$.

This is exactly the situation that takes place for $\nu = 1$ in our model (first line in Fig.24). The dynamic wall is located in the instability region, and the BH-BH phase transition make us land in the area of deconfinement (Fig.24.A,B, first line). So in the absence of the primary anisotropy confinement/deconfinement phase transition is determined by the first order phase transition (BH-BH line) till the intersection with the WL-line, providing us with the crossover. The part of the BH-BH line, that turns out to be in the deconfinement area to the right of the crossover (Fig.22.A,C), seems to cause density jump in the QGP. For large c_B BH-BH phase transition lies above the DW, that is still in the instability region (Fig.24.C, first line). So the entire BH-BH line serves for density jumps in QGP, not separating confinement and deconfinement areas (Fig.22.E).

For $\nu = 4.5$ the situation is quite different, as the dynamic wall is located in the stable region. In the absence of external magnetic field first order phase transition lands into the deconfinement region for $0 \leq \mu \leq 0.2448$, closing the crossover from above till the intersection with the WL-line. For $\mu > 0.2448$ the Hawling-Page-like

phase transition lands in the confinement area (Fig.24.A, second line). This time the BH-BH line produces the density jump of the confined matter, while confinement/deconfinement phase transition is determined by the y -Wilson loop. (Let us remind that for $c_B = 0$ there is no difference between y_1 and y_2 orientations.) On Fig.24.A in the third line show the same picture more clearly, zooming the BH-BH transition to the confinement area from Fig.24.A, second line.

Adding the external magnetic field makes BH-BH line go under the WL-line into the confinement area earlier, i.e. for lesser μ values (Fig.24.B, second line and zoom in Fig.24.B, third line). The curved triangle limited by the intercection point from the left, CEP temperature from the right, BH-BH line from below and WL from above should represent the area of higher density in the confinement area (Fig.22.B,D).

When the coupling coefficient reaches critical value $c_{B\text{crit}} \approx -0.11$ the entire BH-BH line sinks into the confinement area. Therefore the confinement/deconfinement phase transition goes along the Wilson loop line only (Fig.24.C, second line and zoom in Fig.24.C, third line), and we have a higher density sector between the BH-BH and WL-lines (Fig.22.F).

4 Conclusions

In this work holographic description of hot dense anisotropic QGP with heavy quarks in magnetic field for heavy quarks model was constructed. This model is the extension of the previous solution [28] that serves as a zero magnetic field limit.

The magnetic field $F^{(B)}$ is characterized by two parameters – “charge” $F_{xy_1}^{(B)} = q_B$ and metric coupling coefficient c_B . First of them characterises the Maxwell field itself, while the second one describes the metric deformation due to the presence of external magnetic field. In our model kinetic coupling function has simplest gaussian form [25, 34, 40] and depends of the coefficient c_B and the external “charge” q_B which not connected to each other. Such a parameterization was introduced for more generality of the model. As a result, it turns out that the magnetic “charge” is almost not involved into the main properties of our holographic description for QGP, so we actually consider c_B as an efficient factor of the Maxwell field $F_{xy_1}^{(B)}$ and put $q_B = 1$. But this doesn’t mean at all that the phase transition structure is independent from the strength of external magnetic field. The fact is that we can always link these parameters determining coupling coefficient as a function of “charge”, $c_B = f(q_B)$. The specific shape of this function is an important aspect that should allow to fit lattice results, experimental data as well as reach agreement with other theoretical considerations.

The structure of phase transitions strongly depends on the chosen model – models corresponding to light/heavy quarks have different structures. In fact there is

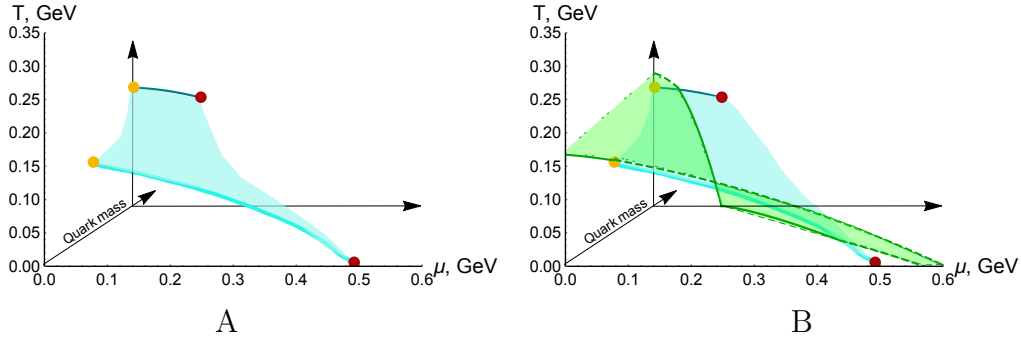


Figure 25. Schematic pictures of phase transitions dependence on quark mass. The cyan surface shows the first order phase transition (A) and green surface shows the confinement/deconfinement transition surface (A, B). The red and yellow points are critical end points.

finer division depending on quark type taken into account, see for example [53–55]. In the holographic approach light/heavy quarks models have different structures of the background phase transition [14, 26]. In most of holographic models the background phase transition, see Fig.25.A, is related to chiral symmetry breaking [13, 20, 22, 31, 32, 38, 39, 41, 45, 46, 48]. Confinement/deconfinement phase transition may be related to background phase transition and may be not, Fig.25.B. This depends on the relative position of the dynamic wall and the background phase transition, see more detail discussion in Sect.3.3. An expected phase structure for the intermediate version of the model between heavy and light quarks (the so-called “hybrid” model) is shown on Fig.25.A and Fig.25.B. The area of the assumed location of the first-order phase transition line is depicted in cyan.

In this paper we investigated the dependence of the phase transition structure on the anisotropy, characterized by parameter ν (see eq.(2.3)), and magnetic fields. Our results are schematically shown in the 3D diagrams (μ, ν, T) and (μ, B, T) on Fig.26. The WL phase transition is indicated by green lines, the BH-BH phase transition is indicated by cyan, blue and magenta lines. The solid lines of BH-BH and WL phase transitions indicate the confinement/deconfinement phase transition. In the figure Fig.26.A we see that while increasing anisotropy, the BH-BH phase transition and WL phase transition occur at lower temperatures for the same values of the chemical potential. With the increase of ν , the first-order phase transition line elongates. In the figure Fig.26.B, we see qualitatively the same situation with increasing magnetic field, the phase transition occurs at lower temperature values for the same chemical potential values, but the first-order phase transition line shortens.

To complete the confinement/deconfinement picture we also investigated string properties of the solution – string tension depending of orientation of the quark

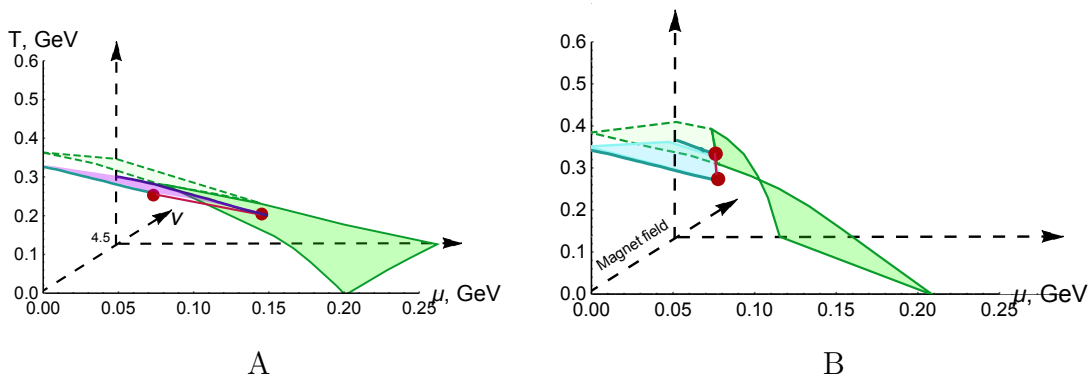


Figure 26. Schematic representations of the structure of phase transitions of a model describing heavy quarks depending on the anisotropy caused by: parameter ν (A), magnetic field (B).

pair. For this purpose we investigated behavior of differently oriented temporal Wilson loops, that determines location of confinement/deconfinement phase transition. Note that unlike the dynamic walls' positions the string tension strongly depends on the integration boundary for the scalar field [44]. Here we performed calculations for the simplest case $z_0 = \epsilon \ll 1$ only. Choice of the function $z_0 = f(z_h)$ will be consider in further investigations of the model.

In the model considered in this paper we have observed only IMC. Such a behavior distinguishes this model from more complicated heavy quarks models with higher order polynomials in the warp-factor. Namely, the model considered in [40] demonstrates MC for small magnetic fields and IMC for large ones. This phenomena takes place for small values of the chemical potential, while for large admissible chemical potentials the model exhibits MC only. Similar to the simplest heavy quarks models [19, 28] the model has CEPs, those position depend on values of magnetic field. It seems, that this phenomena will take place also for the case of the warp factor considered in [34] (see Table 2 in Appendix B.2).

Note, that to get more realistic description of the phase structure we have to deal with so-called hybrid warped factor that is a combination of the exponent of polynomials with logarithmic corrections. Constructing of such a superposition model is a must-have item on the list of future research.

5 Acknowledgments

This work is supported by Russian Science Foundation grant №20-12-00200.

Appendix

A EOM

For $F_{xy_1}^{(B)} = q_B$ the corresponding EOM are the following:

$$\begin{aligned} \phi'' + \phi' \left(\frac{g'}{g} + \frac{3\mathbf{b}'}{2\mathbf{b}} - \frac{\nu+2}{\nu z} + c_B z \right) + \left(\frac{z}{L} \right)^2 \frac{\partial f_1}{\partial \phi} \frac{(A'_t)^2}{2\mathbf{b}g} - \\ - \left(\frac{L}{z} \right)^{2-\frac{4}{\nu}} \frac{\partial f_2}{\partial \phi} \frac{q^2 e^{-c_B z^2}}{2\mathbf{b}g} - \left(\frac{z}{L} \right)^{\frac{2}{\nu}} \frac{\partial f_B}{\partial \phi} \frac{q_B^2}{2\mathbf{b}g} - \left(\frac{L}{z} \right)^2 \frac{\mathbf{b}}{g} \frac{\partial V}{\partial \phi} = 0, \end{aligned} \quad (\text{A.1})$$

$$A_t'' + A_t' \left(\frac{\mathbf{b}'}{2\mathbf{b}} + \frac{f_1'}{f_1} + \frac{\nu-2}{\nu z} + c_B z \right) = 0, \quad (\text{A.2})$$

$$g'' + g' \left(\frac{3\mathbf{b}'}{2\mathbf{b}} - \frac{\nu+2}{\nu z} + c_B z \right) - \left(\frac{z}{L} \right)^2 \frac{f_1 (A'_t)^2}{\mathbf{b}} - \left(\frac{z}{L} \right)^{\frac{2}{\nu}} \frac{q_B^2 f_B}{\mathbf{b}} = 0, \quad (\text{A.3})$$

$$\mathbf{b}'' - \frac{3(\mathbf{b}')^2}{2\mathbf{b}} + \frac{2\mathbf{b}'}{z} - \frac{4\mathbf{b}}{3\nu z^2} \left(1 - \frac{1}{\nu} + \left(1 - \frac{3\nu}{2} \right) c_B z^2 - \frac{\nu c_B^2 z^4}{2} \right) + \frac{\mathbf{b} (\phi')^2}{3} = 0, \quad (\text{A.4})$$

$$2g' \frac{\nu-1}{\nu} + 3g \frac{\nu-1}{\nu} \left(\frac{\mathbf{b}'}{\mathbf{b}} - \frac{4(\nu+1)}{3\nu z} + \frac{2c_B z}{3} \right) + \left(\frac{L}{z} \right)^{1-\frac{4}{\nu}} \frac{L q^2 e^{-c_B z^2} f_2}{\mathbf{b}} = 0, \quad (\text{A.5})$$

$$\begin{aligned} \frac{\mathbf{b}''}{\mathbf{b}} + \frac{(\mathbf{b}')^2}{2\mathbf{b}^2} + \frac{3\mathbf{b}'}{\mathbf{b}} \left(\frac{g'}{2g} - \frac{\nu+1}{\nu z} + \frac{2c_B z}{3} \right) - \frac{g'}{3zg} \left(5 + \frac{4}{\nu} - 3c_B z^2 \right) + \\ + \frac{8}{3z^2} \left(1 + \frac{3}{2\nu} + \frac{1}{2\nu^2} \right) - \frac{4c_B}{3} \left(1 + \frac{3}{2\nu} - \frac{c_B z^2}{2} \right) + \frac{g''}{3g} + \frac{2}{3} \left(\frac{L}{z} \right)^2 \frac{\mathbf{b}V}{g} = 0, \end{aligned} \quad (\text{A.6})$$

where $' = \partial/\partial z$.

For $F_{xy2}^{(B)} = q_B$ the corresponding EOM are the following:

$$\begin{aligned} \phi'' + \phi' \left(\frac{g'}{g} + \frac{3\mathbf{b}'}{2\mathbf{b}} - \frac{\nu+2}{\nu z} + c_B z \right) + \left(\frac{z}{L} \right)^2 \frac{\partial f_1}{\partial \phi} \frac{(A'_t)^2}{2\mathbf{b}g} - \\ - \left(\frac{L}{z} \right)^{2-\frac{4}{\nu}} \frac{\partial f_2}{\partial \phi} \frac{q^2 e^{-c_B z^2}}{2\mathbf{b}g} - \left(\frac{z}{L} \right)^{\frac{2}{\nu}} \frac{\partial f_B}{\partial \phi} \frac{q_B^2 e^{-c_B z^2}}{2\mathbf{b}g} - \left(\frac{L}{z} \right)^2 \frac{\mathbf{b}}{g} \frac{\partial V}{\partial \phi} = 0, \end{aligned} \quad (\text{A.7})$$

$$A_t'' + A_t' \left(\frac{\mathbf{b}'}{2\mathbf{b}} + \frac{f_1'}{f_1} + \frac{\nu-2}{\nu z} + c_B z \right) = 0, \quad (\text{A.8})$$

$$g'' + g' \left(\frac{3\mathbf{b}'}{2\mathbf{b}} - \frac{\nu+2}{\nu z} + c_B z \right) - \left(\frac{z}{L} \right)^2 \frac{f_1 (A'_t)^2}{\mathbf{b}} - \left(\frac{z}{L} \right)^{\frac{2}{\nu}} \frac{q_B^2 e^{-c_B z^2} f_B}{\mathbf{b}} = 0, \quad (\text{A.9})$$

$$\mathbf{b}'' - \frac{3(\mathbf{b}')^2}{2\mathbf{b}} + \frac{2\mathbf{b}'}{z} - \frac{4\mathbf{b}}{3\nu z^2} \left(1 - \frac{1}{\nu} + \left(1 - \frac{3\nu}{2} \right) c_B z^2 - \frac{\nu c_B^2 z^4}{2} \right) + \frac{\mathbf{b}(\phi')^2}{3} = 0, \quad (\text{A.10})$$

$$\begin{aligned} 2g' \frac{\nu-1}{\nu} + 3g \frac{\nu-1}{\nu} \left(\frac{\mathbf{b}'}{\mathbf{b}} - \frac{4(\nu+1)}{3\nu z} + \frac{2c_B z}{3} \right) + \left(\frac{L}{z} \right)^{1-\frac{4}{\nu}} \frac{L q^2 e^{-c_B z^2} f_2}{\mathbf{b}} - \\ - \left(\frac{z}{L} \right)^{\frac{2}{\nu}} \frac{q_B^2 e^{-c_B z^2} z f_B}{\mathbf{b}} = 0, \end{aligned} \quad (\text{A.11})$$

$$\begin{aligned} \frac{\mathbf{b}''}{\mathbf{b}} + \frac{(\mathbf{b}')^2}{2\mathbf{b}^2} + \frac{3\mathbf{b}'}{\mathbf{b}} \left(\frac{g'}{2g} - \frac{\nu+1}{\nu z} + \frac{2c_B z}{3} \right) - \frac{g'}{3zg} \left(5 + \frac{4}{\nu} - 3c_B z^2 \right) + \frac{8}{3z^2} \left(1 + \frac{3}{2\nu} + \frac{1}{2\nu^2} \right) - \\ - \frac{4c_B}{3} \left(1 + \frac{3}{2\nu} - \frac{c_B z^2}{2} \right) + \frac{g''}{3g} + \left(\frac{z}{L} \right)^{\frac{2}{\nu}} \frac{q_B^2 e^{-c_B z^2} f_B}{3\mathbf{b}g} + \frac{2}{3} \left(\frac{L}{z} \right)^2 \frac{\mathbf{b}V}{g} = 0. \end{aligned} \quad (\text{A.12})$$

Note, that the form of the external magnetic field $F_{\mu\nu}^{(B)}$ has influence on the penultimate terms in (A.1, A.7), last terms in (A.3, A.9), equations (A.11, A.12) have an extra term in comparison with (A.5, A.6) correspondingly. Equations (A.2, A.8) on electric field A_t and equations (A.4, A.10) on scalar field ϕ are identical, thus these quantities are invariants with respect to the orientation of the external magnetic field.

The important feature of the systems (A.1–A.6) and (A.7–A.12) is that we can't get a solution for the blackening function from (A.3) or (A.9) immediately after the electric field A_t , as we also need to find or exclude the 3-rd Maxwell field's coupling function f_B first.

It is possible to set f_B manually, but we can avoid such an arbitrariness. Excluding higher derivatives from equations (A.2–A.6) and substituting them into (A.1),

we get the following expression for the coupling function f_B :

$$f_B = 2 \left(\frac{z}{L} \right)^{-\frac{2}{\nu}} \mathfrak{b}g \frac{c_B z}{q_B^2} \left(\frac{3\mathfrak{b}'}{2\mathfrak{b}} - \frac{2}{\nu z} + c_B z + \frac{g'}{g} \right). \quad (\text{A.13})$$

Similarly excluding higher derivatives from equations (A.8–A.12) and substituting them into (A.6), we get the following expression for the coupling function f_B :

$$f_B = -2 \left(\frac{z}{L} \right)^{-\frac{2}{\nu}} e^{c_B z^2} \mathfrak{b}g \frac{c_B z}{q_B^2} \left(\frac{3\mathfrak{b}'}{2\mathfrak{b}} - \frac{2}{\nu z} + c_B z + \frac{g'}{g} \right). \quad (\text{A.14})$$

B Tables

Here we present phase diagrams for various holographic heavy quarks models. In Table 1 we collected known results for zero magnetic field and in Table 2 the results for $B \neq 0$.

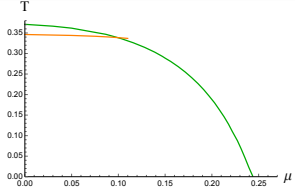
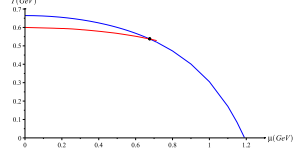
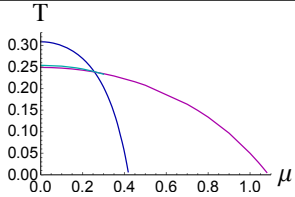
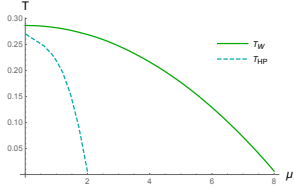
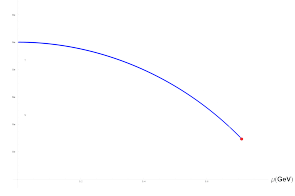
HQCD heavy quarks models show different behavior for different polynomials in warped factor and function $f(z)$: the plot in the cell (11) of Table 2, that corresponds to the simplest warp factor, shows the IMC, i.e. the critical temperature decreases with increasing $|c_B|$, that corresponds to increasing the magnetic field. This is in the opposite with lattice simulations for heavy quarks that reveal the MC phenomenon [65–67].

The deformation of the warp-factor by adding dz^5 changes IMC to MC for d large enough, see plot in the cell (3,3) of Table 2. If one considers a deformation by quadratic factor pz^4 , then for particular p , suitable to fit Regge spectrum, one gets MC for small and medium B , meanwhile one observes IMC for large B , see plot in cell (3,2).

We also see the change of regime from IMC to MC for large enough μ , see plots in the cell (1,3).

B.1

Table 1. Holographic models for heavy quarks without magnetic field.

$B = 0$	Heavy quarks		
\mathcal{A}	$-cz^2$	$-cz^2 + pz^4$	$-cz^2 + dz^5$
$\nu = 1$ $f_1(z) = 1$	 [28]	 [19]	
$\nu = 4.5$ $f_1 = z^{2-2/\nu}$	 [28, 44]	-	-
$\nu = 1$ $f_1 = e^{c_1 z^2}$	 [34]	 [19]	-
$\nu \neq 1$ $f_1 = z^{2-2/\nu} e^{c_1 z^2}$	-	-	-

B.2

Table 2. Holographic models for heavy quarks in magnetic field.

$B \neq 0$	Heavy quarks		
\mathcal{A}	$-cz^2$	$-cz^2 + pz^4$	$-cz^2 + dz^5$
$\nu = 1$ $f_1(z) = 1$		-	-
		-	-
	see Fig.22	-	-
$\nu = 4.5$ $f_1 = z^{2-2/\nu}$		-	-
		-	-
$\nu = 1$ $f_1 = e^{c_1 z^2}$			
		-	-
$\nu \neq 1$ $f_1 = z^{2-2/\nu} e^{c_1 z^2}$	-	-	-

References

- [1] J. Casalderrey-Solana, H. Liu, D. Mateos, K. Rajagopal and U. A. Wiedemann, “Gauge/String Duality, Hot QCD and Heavy Ion Collisions”, Cambridge University Press (2014) [arXiv:1101.0618 [hep-th]].
- [2] I. Ya. Aref’eva, “Holographic approach to quark-gluon plasma in heavy ion collisions”, Phys. Usp. **57**, 527 (2014).
- [3] O. DeWolfe, S. S. Gubser, C. Rosen and D. Teaney, “Heavy ions and string theory”, Prog. Part. Nucl. Phys. **75**, 86 (2014) [arXiv:1304.7794 [hep-th]].
- [4] O. Andreev and V. I. Zakharov, “On Heavy-Quark Free Energies, Entropies, Polyakov Loop, and AdS/QCD,” JHEP **04**, 100 (2007) [arXiv:hep-ph/0611304 [hep-ph]].
- [5] U. Gursoy, E. Kiritsis, L. Mazzanti and F. Nitti, “Holography and Thermodynamics of 5D Dilaton-gravity”, JHEP, **0905**, 033 (2009) [arXiv:0812.0792 [hep-th]].
- [6] U. Gursoy, E. Kiritsis, L. Mazzanti and F. Nitti, “Improved Holographic Yang-Mills at Finite Temperature: Comparison with Data,” Nucl. Phys. B **820**, 148-177 (2009) [arXiv:0903.2859 [hep-th]].
- [7] S. He, M. Huang and Q. S. Yan, “Logarithmic correction in the deformed AdS_5 model to produce the heavy quark potential and QCD beta function”, Phys. Rev. D **83**, 045034 (2011) [arXiv:1004.1880 [hep-ph]].
- [8] M. Mia, K. Dasgupta, C. Gale and S. Jeon, “Heavy Quarkonium Melting in Large N Thermal QCD”, Phys. Lett. B **694**, 460-466 (2011) [arXiv:1006.0055 [hep-th]].
- [9] U. Gursoy, E. Kiritsis, L. Mazzanti, G. Michalogiorgakis and F. Nitti, “Improved Holographic QCD,” Lect. Notes Phys. **828**, 79-146 (2011) [arXiv:1006.5461 [hep-th]].
- [10] P. Colangelo, F. Giannuzzi, S. Nicotri and V. Tangorra, “Temperature and quark density effects on the chiral condensate: An AdS/QCD study,” Eur. Phys. J. C **72**, 2096 (2012) [arXiv:1112.4402 [hep-ph]].
- [11] R. G. Cai, S. He and D. Li, “A hQCD model and its phase diagram in Einstein-Maxwell-Dilaton system,” JHEP **03**, 033 (2012) [arXiv:1201.0820 [hep-th]].
- [12] D. Giataganas, “Probing strongly coupled anisotropic plasma,” JHEP **07**, 031 (2012) [arXiv:1202.4436 [hep-th]].
- [13] D. Li, M. Huang and Q. S. Yan, “A dynamical soft-wall holographic QCD model for chiral symmetry breaking and linear confinement,” Eur. Phys. J. C **73**, 2615 (2013) [arXiv:1206.2824 [hep-th]].
- [14] S. He, S. Y. Wu, Y. Yang and P. H. Yuan, “Phase Structure in a Dynamical Soft-Wall Holographic QCD Model,” JHEP **04**, 093 (2013) [arXiv:1301.0385 [hep-th]].
- [15] D. Li and M. Huang, “Dynamical holographic QCD model for glueball and light meson spectra,” JHEP **11**, 088 (2013) [arXiv:1303.6929 [hep-ph]].

- [16] Y. Yang and P. H. Yuan, “A Refined Holographic QCD Model and QCD Phase Structure,” *JHEP* **11**, 149 (2014) [arXiv:1406.1865 [hep-th]].
- [17] D. Li, S. He and M. Huang, “Temperature dependent transport coefficients in a dynamical holographic QCD model,” *JHEP* **06**, 046 (2015) [arXiv:1411.5332 [hep-ph]].
- [18] R. Rougemont, R. Critelli and J. Noronha, “Holographic calculation of the QCD crossover temperature in a magnetic field”, *Phys. Rev.* **D93**, 045013 (2015) [arXiv:1505.07894 [hep-ph]].
- [19] Y. Yang and P. H. Yuan, “Confinement-deconfinement phase transition for heavy quarks in a soft wall holographic QCD model,” *JHEP* **12**, 161 (2015) [arXiv:1506.05930 [hep-th]].
- [20] K. Chelabi, Z. Fang, M. Huang, D. Li and Y. L. Wu, “Realization of chiral symmetry breaking and restoration in holographic QCD,” *Phys. Rev. D* **93**, no.10, 101901 (2016) [arXiv:1511.02721 [hep-ph]].
- [21] Z. Fang, S. He and D. Li, “Chiral and Deconfining Phase Transitions from Holographic QCD Study,” *Nucl. Phys. B* **907** (2016), 187-207 [arXiv:1512.04062 [hep-ph]].
- [22] K. Chelabi, Z. Fang, M. Huang, D. Li and Y. L. Wu, “Chiral Phase Transition in the Soft-Wall Model of AdS/QCD,” *JHEP* **04**, 036 (2016) [arXiv:1512.06493 [hep-ph]].
- [23] D. Li, M. Huang, Y. Yang and P. H. Yuan, “Inverse Magnetic Catalysis in the Soft-Wall Model of AdS/QCD,” *JHEP* **02**, 030 (2017) [arXiv:1610.04618 [hep-th]].
- [24] D. Li and M. Huang, “Chiral phase transition of QCD with $N_f = 2 + 1$ flavors from holography,” *JHEP* **02**, 042 (2017) [arXiv:1610.09814 [hep-ph]].
- [25] D. Dudal and S. Mahapatra, “Confining gauge theories and holographic entanglement entropy with a magnetic field,” *JHEP* **04**, 031 (2017) [arXiv:1612.06248 [hep-th]].
- [26] M.-W. Li, Y. Yang, P.-H. Yuan, “Approaching Confinement Structure for Light Quarks in a Holographic Soft Wall QCD Model”, *Phys. Rev. D* **96**, 066013 (2017), [arXiv:1703.09184 [hep-th]].
- [27] Y. Yang and P. H. Yuan, “Universal Behaviors of Speed of Sound from Holography,” *Phys. Rev. D* **97**, no.12, 126009 (2018) [arXiv:1705.07587 [hep-th]].
- [28] I. Ya. Aref’eva and K. A. Rannu, “Holographic Anisotropic Background with Confinement-Deconfinement Phase Transition”, *JHEP* **05**, 206 (2018), [arXiv:1802.05652 [hep-th]].
- [29] I. Y. Aref’eva, A. A. Golubtsova and G. Policastro, “Exact holographic RG flows and the $A_1 \times A_1$ Toda chain,” *JHEP* **05**, 117 (2019) [arXiv:1803.06764 [hep-th]].
- [30] I. Aref’eva, K. Rannu and P. Slepov, “Orientation Dependence of Confinement-Deconfinement Phase Transition in Anisotropic Media,” *Phys. Lett. B* **792**, 470-475 (2019) [arXiv:1808.05596 [hep-th]].

- [31] Z. Fang, Y. L. Wu and L. Zhang, “Chiral phase transition and QCD phase diagram from AdS/QCD,” *Phys. Rev. D* **99** (2019) no.3, 034028 [arXiv:1810.12525 [hep-ph]].
- [32] Jianwei Chen, Song He, Mei Huang, Danning Li, “Critical exponents of finite temperature chiral phase transition in soft-wall AdS/QCD models”, arXiv:1810.07019 [hep-ph].
- [33] A. A. Golubtsova and V. H. Nguyen, “Wilson Loops in Exact Holographic RG Flows at Zero and Finite Temperatures,” *Theor. Math. Phys.* **202**, no.2, 214-230 (2020) [arXiv:1906.12316 [hep-th]].
- [34] H. Bohra, D. Dudal, A. Hajilou and S. Mahapatra, “Anisotropic string tensions and inversely magnetic catalyzed deconfinement from a dynamical AdS/QCD model”, *Phys. Lett. B* **801**, 135184 (2020) [arXiv:1907.01852 [hep-th]].
- [35] X. Chen, D. Li, D. Hou and M. Huang, “Quarkyonic phase from quenched dynamical holographic QCD model,” *JHEP* **03** (2020), 073 [arXiv:1908.02000 [hep-ph]].
- [36] I. Aref’eva, K. Rannu and P. Slepov, “Cornell potential for anisotropic QGP with non-zero chemical potential”, *EPJ Web Conf.* **222**, 03023 (2019)
- [37] Z. Fang and Y. L. Wu, “Equation of state and chiral transition in soft-wall AdS/QCD with more realistic gravitational background,” [arXiv:1909.06917 [hep-ph]].
- [38] Z. Fang and L. Zhang, “Chiral transition and meson melting with finite chemical potential in an improved soft-wall AdS/QCD Model,” [arXiv:1910.02269 [hep-ph]].
- [39] A. Ballon-Bayona and L. A. H. Mamani, “Nonlinear realization of chiral symmetry breaking in holographic soft wall models,” *Phys. Rev. D* **102** (2020) no.2, 026013 [arXiv:2002.00075 [hep-ph]].
- [40] S. He, Y. Yang and P. H. Yuan, “Analytic Study of Magnetic Catalysis in Holographic QCD”, [arXiv:2004.01965 [hep-th]].
- [41] A. Ballon-Bayona, J. P. Shock and D. Zoakos, “Magnetic catalysis and the chiral condensate in holographic QCD,” [arXiv:2005.00500 [hep-th]].
- [42] A. Ballon-Bayona, H. Boschi-Filho, E. Folco Capossoli and D. M. Rodrigues, “Criticality from EMD holography at finite temperature and density,” [arXiv:2006.08810 [hep-th]].
- [43] P. Colangelo, F. De Fazio and N. Losacco, “Chaos in a $Q\bar{Q}$ system at finite temperature and baryon density,” *Phys. Rev. D* **102**, no.7, 074016 (2020) [arXiv:2007.06980 [hep-ph]].
- [44] I. Y. Aref’eva, K. Rannu and P. Slepov, “Holographic Anisotropic Model for Light Quarks with Confinement-Deconfinement Phase Transition,” [arXiv:2009.05562 [hep-th]].
- [45] M. W. Li, Y. Yang and P. H. Yuan, “Analytic Study on Chiral Phase Transition in Holographic QCD,” [arXiv:2009.05694 [hep-th]].

- [46] H. Bohra, D. Dudal, A. Hajilou and S. Mahapatra, “Chiral transition in the probe approximation from an Einstein-Maxwell-dilaton gravity model,” [arXiv:2010.04578 [hep-th]].
- [47] I. Ya. Aref’eva, “Holography for nonperturbative study of QFT”, Phys. Part. Nucl. **51**, no.4, 489-496 (2020)
- [48] D. M. Rodrigues, D. Li, E. Folco Capossoli and H. Boschi-Filho, “Finite density effects on chiral symmetry breaking in a magnetic field in 2+1 dimensions from holography,” [arXiv:2010.06762 [hep-th]].
- [49] N. Jokela and J. G. Subils, “Is entanglement a probe of confinement?,” [arXiv:2010.09392 [hep-th]].
- [50] I. Ya. Aref’eva, “Theoretical studies of the formation and properties of quark-gluon matter under conditions of high baryon densities attainable at the NICA experimental complex”, submitted to Phys. Part. Nucl.
- [51] P. Slepov, “A way to improve string tension dependence on temperature in holographic mode”, submitted to Phys. Part. Nucl.
- [52] K. Rannu, “Holographic Anisotropic Model for Light Quarks with Confinement-Deconfinement Phase Transition”, submitted to Phys. Part. Nucl.
- [53] F. R. Brown, F. P. Butler, H. Chen, N. H. Christ, Z. h. Dong, W. Schaffer, L. I. Unger and A. Vaccarino, “On the existence of a phase transition for QCD with three light quarks,” Phys. Rev. Lett. **65**, 2491-2494 (1990)
- [54] O. Philipsen and C. Pinke, “The $N_f = 2$ QCD chiral phase transition with Wilson fermions at zero and imaginary chemical potential,” Phys. Rev. D **93**, no.11, 114507 (2016) [arXiv:1602.06129 [hep-lat]].
- [55] O. Philipsen, PoS **LATTICE2019**, 273 (2019) [arXiv:1912.04827 [hep-lat]].
- [56] V. Skokov, A. Y. Illarionov and V. Toneev, “Estimate of the magnetic field strength in heavy-ion collisions,” Int. J. Mod. Phys. A **24**, 5925-5932 (2009) [arXiv:0907.1396 [nucl-th]].
- [57] V. Voronyuk, V. D. Toneev, W. Cassing, E. L. Bratkovskaya, V. P. Konchakovski and S. A. Voloshin, “(Electro-)Magnetic field evolution in relativistic heavy-ion collisions,” Phys. Rev. C **83**, 054911 (2011) [arXiv:1103.4239 [nucl-th]].
- [58] A. Bzdak and V. Skokov, “Event-by-event fluctuations of magnetic and electric fields in heavy ion collisions,” Phys. Lett. B **710**, 171-174 (2012) [arXiv:1111.1949 [hep-ph]].
- [59] W. T. Deng and X. G. Huang, “Event-by-event generation of electromagnetic fields in heavy-ion collisions,” Phys. Rev. C **85**, 044907 (2012) [arXiv:1201.5108 [nucl-th]].
- [60] V. Toneev, O. Rogachevsky and V. Voronyuk, “Evidence for creation of strong electromagnetic fields in relativistic heavy-ion collisions,” Eur. Phys. J. A **52**, no.8, 264 (2016) [arXiv:1604.06231 [hep-ph]].

- [61] K. Enqvist and P. Olesen, “On primordial magnetic fields of electroweak origin,” *Phys. Lett. B* **319**, 178-185 (1993) [arXiv:hep-ph/9308270 [hep-ph]].
- [62] D. Grasso and H. R. Rubinstein, “Magnetic fields in the early universe,” *Phys. Rept.* **348**, 163-266 (2001) [arXiv:astro-ph/0009061 [astro-ph]].
- [63] S. Mereghetti, J. Pons and A. Melatos, “Magnetars: Properties, Origin and Evolution,” *Space Sci. Rev.* **191**, no.1-4, 315-338 (2015) [arXiv:1503.06313 [astro-ph.HE]]
- [64] R. Turolla, S. Zane and A. Watts, “Magnetars: the physics behind observations. A review,” *Rept. Prog. Phys.* **78**, no.11, 116901 (2015) [arXiv:1507.02924 [astro-ph.HE]].
- [65] M. D’Elia, S. Mukherjee and F. Sanfilippo, “QCD Phase Transition in a Strong Magnetic Background,” *Phys. Rev. D* **82**, 051501 (2010) [arXiv:1005.5365 [hep-lat]].
- [66] E. M. Ilgenfritz, M. Kalinowski, M. Muller-Preussker, B. Petersson and A. Schreiber, “Two-color QCD with staggered fermions at finite temperature under the influence of a magnetic field,” *Phys. Rev. D* **85**, 114504 (2012) [arXiv:1203.3360 [hep-lat]].
- [67] M. D’Elia, “Lattice QCD Simulations in External Background Fields,” *Lect. Notes Phys.* **871**, 181-208 (2013) [arXiv:1209.0374 [hep-lat]].
- [68] M. Strickland, “Thermalization and isotropization in heavy-ion collisions”, *Pramana* **84**, 671 (2015).
- [69] J. Adam *et al.* [ALICE Collaboration], “Centrality dependence of the charged-particle multiplicity density at midrapidity in Pb-Pb collisions at $\sqrt{s_{NN}} = 5.02$ TeV”, *Phys. Rev. Lett.* **116**, no. 22, 222302 (2016) [arXiv:1512.06104 [nucl-ex]].
- [70] I. Y. Aref’eva and A. A. Golubtsova, “Shock waves in Lifshitz-like spacetimes”, *JHEP* **04**, 011 (2015) [arXiv:1410.4595 [hep-th]].
- [71] I. Y. Aref’eva, A. Patrushev and P. Slepov, “Holographic entanglement entropy in anisotropic background with JHEP **07**, 043 (2020) [arXiv:2003.05847 [hep-th]].
- [72] D. S. Ageev, I. Y. Aref’eva, A. A. Golubtsova and E. Gourgoulhon, “Thermalization of holographic Wilson loops in spacetimes with spatial anisotropy,” *Nucl. Phys. B* **931**, 506-536 (2018) [arXiv:1606.03995 [hep-th]].
- [73] K. B. Fadafan and R. Morad, “Jets in a strongly coupled anisotropic plasma”, *Eur. Phys. J. C* **78**, 16 (2018) [arXiv:1710.06417 [hep-th]].
- [74] U. Gursoy, I. Iatrakis, M. Jarvinen and G. Nijs, “Inverse Magnetic Catalysis from improved Holographic QCD in the Veneziano limit”, *JHEP* **03**, 053 (2017) [arXiv:1611.06339 [hep-th]].
- [75] U. Gursoy, M. Jarvinen and G. Nijs, “Holographic QCD in the Veneziano limit at finite Magnetic Field and Chemical Potential”, *Phys. Rev. Lett.* **120**, 242002 (2018) [arXiv:1707.00872 [hep-th]].

- [76] U. Gursoy, M. Jarvinen, G. Nijs and J. F. Pedraza, “Inverse Anisotropic Catalysis in Holographic QCD”, *Phys. Rev. Lett.* **04**, 071 (2019) [arXiv:1811.11724 [hep-th]].